Ocean Modelling 179 (2022) 102122

Contents lists available at ScienceDirect

Ocean Modelling

journal homepage: www.elsevier.com/locate/ocemod

Large eddy simulation of focused breaking waves with different wave steepness

Ting Cui [a,b,c], Guanghua He [b], Meirong Jiang [d], Weizhi Wang [c,*], Lihao Yuan [a], Duanfeng Han [a], Arun Kamath [c], Hans Bihs [c]

[a] College of Shipbuilding Engineering, Harbin Engineering University, Harbin 150001, China
[b] School of Ocean Engineering, Harbin Institute of Technology, Weihai 264209, China
[c] Department of Civil and Environmental Engineering, Norwegian University of Science and Technology, Høgskoleringen 7A, 7491 Trondheim, Norway
[d] CNOOC Research Institute Co., Ltd., Beijing 100028, China

ARTICLE INFO

Keywords:
Breaking waves
Local wave steepness
Splash-up
Air entrainment
Energy dissipation
Turbulence intensity

ABSTRACT

The profile of fluid field and wave geometry, kinematic and dynamic characteristics of focused breaking waves in finite water depth with different wave steepness are studied with a constant wave steepness wave focusing method in this paper. The flow field is solved by the two-phase flow model in REEF3D based on the incompressible Navier–Stokes equation and the Large Eddy Simulation (LES) model to simulate the complex breaking process. The numerical model is validated by comparing wave elevation of both focused non-breaking and breaking case with the experimental results and satisfactory agreements are achieved. A series of simulation cases with different global steepness are carried out to analyze the focused waves of different breaking types. The difference between the preset focused condition and the real ones and the area of air cavity rolled by the wave jets are both indicates that the process of wave focusing and breaking show a strong nonlinear profile. The maximum values of the horizontal velocity occur after the impingement moment and can reach 2.5 C_p for extreme steep waves. Three typical wave breaking criteria in finite water depth are calculated and discussed successively. For the geometric criterion analysis, the global wave steepness and local steepness have a good performance both for predicting wave breaking and presenting the breaking intensity. The kinematic breaking criterion ratio shows that the previous threshold 1 at the breaking incipient scenario is not sufficient to predict the wave breaking. Besides, it is found that the time interval when the kinematic breaking criterion ratio big than 1 may related to the wave breaking type. The energy changing rate for both the focusing and dissipation processes increase linearly with the global wave steepness and show a good ability as a dynamic breaking criterion and also prove the asymmetric profile of breaking waves.

1. Introduction

Wave breaking, as an important ocean phenomenon of the surface gravity waves, plays a significant role in momentum and energy transformation around the air–water interface, the generation of the surface current, turbulence mixing both in air and water phase, and wave–offshore structure interaction (Rapp et al., 1990; Bonmarin, 1989; Melville, 1996). Wave breaking in different intensities will produce different breaking profiles and have different wave loads and damages on offshore structures. The accurate estimation of the strong nonlinear wave geometry and kinematic field parameters plays an important role in the prediction of the breaking wave loads on offshore structures. However, less attention has been paid to the understanding of the detailed wave-breaking process and hydrodynamic profiles. Thus, it is critical and meaningful to carry out fundamental research on the breaking waves, especially for the prediction onset of the breaking, geometry profile, enhanced kinematics description, and energy dissipation.

Many significant research works have been made to give a primary introduction of the wave breaking process and provide a more detailed fundamental physical understanding of wave breaking under different water depths. A remarkable laboratory of focused wave breaking performed by Rapp et al. (1990) presented the process of the air–water mixing evolution and showed that spilling breakers experience 10% energy flux changing to as much as 25% for plunging breakers. Based on the air–water gas transfer, Lamarre (1993) reported a series of experiments on air-entrainment measurements by wave breaking (Lamarre and Melville, 1991). Banner and Peregrine (1993) provided fundamental research of velocity field and local geometry profile of plunging breakers in deep water. Duncan (2001) reviewed spilling breakers and

* Corresponding author.
E-mail address: weizhi.wang@ntnu.no (W. Wang).

https://doi.org/10.1016/j.ocemod.2022.102122
Received 7 March 2022; Received in revised form 27 August 2022; Accepted 18 September 2022
Available online 23 September 2022

studied the surface tension influence on wave breaking. A systematic review of the overall process of wave breaking was given by Perlin et al. (2013) for an understanding of the breaking physical process in deep and intermediate water depth. Although wave steepness is a crucial and controllable geometry parameter for focused breaking waves, few studies took it as control and consecutive variables to analyze different wave breaking criteria and other wave profiles under different wave-breaking intensities. The essential aim of this paper is to explore the applicability of three typical breaking criteria, wave geometry profile, kinematics, and energy dissipations under different wave breaking intensities even for extreme steep breaking waves.

a. Analysis of breaking wave characteristics

Numerous studies have been performed to provide credible and accurate fundamental reviews on geometry profiles of wave breaking. Duncan et al. (1999) summarized the crest profile evolution of the gentle spilling breakers with dispersive focusing mechanics. Tian et al. (2010) conducted several experiments of unsteady plunging breakers and defined a local wave steepness to predict breaking onset. On this basis, Tian et al. (2012) adopted an eddy viscosity model for wave-breaking simulations and got reasonable results with their measurements. Alagan Chella et al. (2015) analyzed the asymmetry profiles of breaking waves and found that the water depth has a significant influence on breaking type and other geometry properties. The above studies include research of wave surface elevation and geometry profiles under different breaking types, however, the discussions of the geometry profile variation versus different breaking types and wave steepness are seldom mentioned.

The estimation of the velocity and kinematic field is crucial for the analysis of wave loads on structures.

Grue et al. (2003) defined a new reference fluid velocity profile by a third-order monochromatic Stokes wave beneath the wave surface for steep wave events in deep water. Lim et al. (2015) gave a detailed description of the kinematic field and the variation of the velocity during plunging breaker occurring. Alberello and Iafrati (2019) used the PIV (particle image velocimetry) to capture the kinematic field during breaking. Na et al. (2020) found that the maximum horizontal velocity reached 1.5 times wave phase speed after the onset of spilling breaking waves. The comparison of velocity field under different breaking types and the further discussion of the velocity field evolution under extreme steep waves are still worth the time and efforts. Since the process of wave breaking is chaotic and has large energy transformation, the turbulent profile and vorticity field were only mentioned on several Lubin and Glockner (2015). Based on these previous studies, the further and detailed analysis of wave characteristics and an quantical description of the breaking process versus different breaking intensity is a successively and orderly investigated.

b. Breaking criterion

Some researchers mentioned some parameters for prediction of wave breaking onsets (Banner and Peregrine, 1993; Perlin et al., 2013) and intensity (Tian et al., 2010; Song and Banner, 2002). The research carried out by Bonmarin (1989), Duncan and Longuet-Higgins (1981) and Ramberg and Griffin (1987) were compared with the Stokes theory geometry breaking limitation and found that the experimental limiting wave steepness at breaking incipient section is less than theoretical ones. Rapp et al. (1990) proposed the definition of global wave steepness firstly. Tian et al. (2010) used the spectrally weighted wavenumber, k_s instead of the wavenumber associated with the center frequency of wave group in Rapp and Melville's analysis and they found the breaking onset predictions using the global wave steepness based on their results.

Stansell and MacFarlane (2002) presented the influence of the estimation method of phase speed on predicting wave breaking onset and concluded that the ratio of the horizontal particle velocity and local wave phase speed exceed 1 $|\vec{U}|/C_p \geq 1$ at the incipient scenario is not a necessary condition for breaking. In Wu and Nepf (2002) paper, they summarized previous studies (Baldock et al., 1996; Stansell and MacFarlane, 2002) about the estimation method of the wave phase speed and pointed out that the propagation direction and bandwidth have an influence on the results when choosing different wave phase speed estimation method. Wu and Nepf (2002) adopted the linear wave assumption with an error of 5%∼20%.

Melville (1994) estimated the energy dissipation rate during breaking and found that the energy dissipation rate increases with the wave steepness. In Tian et al. (2010) paper, they found that the normalized energy dissipation closely correlates with global steepness, and the wave group of large global steepness might result in larger energy dissipation. Lim et al. (2015) carried out experiments in three dimensions and found that the wave direction had apparent effects on the geometric breaking criterion and had little effect on the kinematic criterion but they did not drawn conclusions on the dynamic criterion due to its dependency on the wave gauge locations. Wu and Nepf (2002) used the proportion of the higher harmonic frequency energy band of the entire spectrum as the breaking dynamic criterion and found that the energy of the higher-frequency band is sensitive to the choice of the reference location. So the breaking criterion based on the estimation of the energy proportion of the higher frequency is not appropriate and credible to predict wave breaking compared with the geometry and kinematic criterion.

As summarized from the above literature, a systematic analysis of the breaking parameter and breaking criteria including geometry, kinematic, and dynamics sections is necessary and complex work. To achieve a systematic analysis, we carried out a series of simulations of focused breaking waves with the constant steepness method to investigate wave characteristics as the variation of global wave steepness. The numerical model and wave generation method are proposed in Section 2. In Section 3, we compare our results with the experimental data and validate the numerical model. The analysis of the wave parameters and breaking criteria represent a clear framework of this study. The discussion focuses on two subsection, one is the wave characteristic analysis including geometry, kinematic field and quantical description of breaking process, another is the three typical breaking criteria. Finally, in the conclusion section, a summary of the wave profile versus the continued increase wave steepness is depicted.

2. Numerical method and wave tank setup

2.1. Governing equations

The two-phase flow numerical wave tank is built based on the open-source model REEF3D::CFD (Bihs et al., 2016). The flow field for both air and water phase are governed by mass conservation and incompressible Navier–Stokes momentum equation.

$$\frac{\partial u_i}{\partial x_i} = 0 \tag{1}$$

$$\frac{\partial u_i}{\partial t} + u_j \frac{\partial u_i}{\partial x_j} = -\frac{1}{\rho}\frac{\partial P}{\partial x_i} + \frac{\partial}{\partial x_j}\left[\nu_{eff}\left(\frac{\partial u_i}{\partial x_j} + \frac{\partial u_j}{\partial x_i}\right)\right] + g_i + \sigma k \frac{\partial \phi}{\partial x_i} \tag{2}$$

where u_i is velocity vector (u_1, u_2, u_3) in three axis directions (x, y, z), t is the time section, ρ represents the fluid density, P is pressure. The surface tension are considered in this governing equation as the air flow having significant effects on wave breaking process. σ is the surface tension coefficient, k is the mean curvature of free-surface, ϕ is the level set signed distance function $\phi(\vec{x}, t)$ to be introduced later. g is the gravity acceleration. ν_{eff} represents the fluid effective kinematic viscosity $\nu_{eff} = \nu + \nu_t$, including the fluid molecular kinematic viscosity ν and ν_t the turbulence eddy viscosity.

The detailed information of the turbulence and vortex in both air and water are modeled by the large-eddy simulation (LES) models. Based on the definition of LES model, the length scale is the threshold of eddy size. The eddies smaller than the length scale are modeled by the subgrid stress model introduced later and the large energetic eddie are

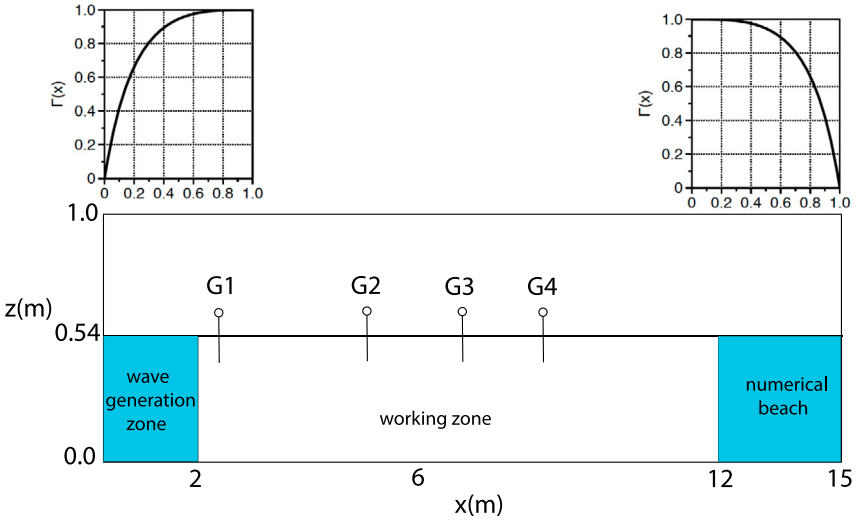

Fig. 1. Diagram of the numerical wave tank physical setting and boundary condition.

resolved by the spatially filtered Navier–Stokes equations. The filtered Navier–Stokes equations are expressed as follows:

$$\frac{\partial \overline{u_i}}{\partial t} + \frac{\partial \overline{u_i}\overline{u_j}}{\partial x_i} = -\frac{1}{\rho}\frac{\partial \overline{p}}{\partial x_i} - \frac{\partial \tau_{ij}}{\partial x_i} + \frac{\partial}{\partial x_j}\left[\nu\left(\frac{\partial \overline{u_i}}{\partial x_j} + \frac{\partial \overline{u_j}}{\partial x_i}\right)\right] + g_i', \tag{3}$$

where $\overline{u}_i$ represents the filtering velocity, $u = \overline{u} + u'$, u' is the residual field, $\overline{u}(x) = \int G(x, x')u(x')\,\mathrm{d}x'$, with G the filter function. The box kernel filter is adopted, characterized by the length scale $\Delta = \sqrt[3]{dxdydz}$, which represents a threshold for the size of eddies. dx, dy, dz are grid sizes in three directions. Eddies larger than Δ are calculated and resolved directly, whereas smaller eddies are modeled. τ_{ij} is the subgrid scale stress, $\tau_{ij} = \overline{u_i u_j} - \overline{u_i}\,\overline{u_j}$.

The Smagorinsky (SGS) model (Hodges et al., 1962) is adopted as subgrid-scale model:

$$\tau_{ij} - \frac{1}{3}\tau_{kk}S_{ij} = \nu_t\left(\frac{\partial \overline{u_i}}{\partial x_j} + \frac{\partial \overline{u_j}}{\partial x_i}\right) = 2\nu_t\overline{S}_{ij}, \tag{4}$$

where the eddy viscosity $\nu_t = C_s^2\Delta^2\left|\overline{S}\right|$ and $\left|\overline{S}\right| = \left(\overline{S}_{ij}\overline{S}_{ij}\right)^{\frac{1}{2}}$; S_{ij} represent the strain rate of the large scale field, C_s is model parameter usually taken as 0.1. Many SGS models have been proposed to model the effects of sub-grid scale motion (Gao et al., 2020), and here we choose the most widely used Smagorinsky model with constant eddy viscosity. The details about the two-phase flow model and numerical method used in this study are presented in Appendix A part.

2.2. Numerical wave tank setup

The numerical model is validated by simulating the experiments by Tian and Choi (2013) at (KAIST), Korea. The experiments of two-dimensional plunging breaking waves were carried out in a narrow wave tank, which is 15 m long, 1.5 m wide, and has a water depth of 0.54 m. The same setup conditions are adopted in a numerical two-dimensional wave tank to reproduce the breaking waves in the experiment. Fig. 1 depicts the wave tank setting according to the experimental physical setup. The computational domain is 15 m long with a constant water depth of 0.54 m. The total numerical wave tank height is 1 m including both air and water phases. A relaxation zone of 2 m is located at the inlet boundary for wave generation and a numerical wave beach is located at the end of the bank with the length of 3 m to absorb wave and prevent wave reflection correspondingly. To replicate the results, the wave gauges are set at the same position as the experiments. The wave gauges locates at $x = 2.84$ m, $x = 5.13$ m, $x = 7.04$ m and $x = 9.07$ m recorded as $G1$, $G2$, $G3$ and $G4$ in sequence.

Two reference cases are set and reproduced as the same wave conditions as the experiments and wave groups DF1 for the focused non-breaking waves condition with global wave steepness as 0.25 and 0.57 for DF2 the focused breaking wave case. The predetermined focused time and location for these two cases are set based on Tian's experiment (Tian and Choi, 2013). There are 128 sinusoidal wave components in the dispersive focusing wave groups with uniform frequency bands ranging from 1.0 Hz to 2.4 Hz, spectral peak frequency, and center frequency as $F_p = 1.1$ and $F_c = 1.7$ separately. The global wave steepness is 0.25 for the non-breaking wave group DF1 and 0.57 for the breaking wave group DF2 respectively. The details of the wave parameters associated with the wave groups are list in Table 3. In this study, the global wave steepness is adjusted for each of the wave groups ranging from 0.25 to 0.75 with an interval of 0.05 that lead to both non-breaking and breaking waves with different breaking types and strengths. Besides the reference case DF2, the predetermined focused location and time are kept the same to analyze the effect of nonlinear amplitude on the focused mechanics.

The frequency bandwidth ratio F_{range}/F_c was kept the same for all cases in this study. Previous research show that the global steepness is highly related to the breaking strength. As for the above summaries, we change the value of the global steepness to investigate the breaking strength, local geometries of breaking waves, kinetic characteristics, momentum flux dissipation, and turbulence profile under different global wave steepness and wave breaking types. X_f and T_f are the predicted focused focal point and focusing time determined by linear theory in Eq. (7). The instant focused position and time for validation case DF2 are 6.25 m and 23.55 s. Besides this case, the focused position and time are set the same for other cases as 7 m and 25 s separately in this study. In this study, the classification of breaking type changing from non-breaking wave, incipient breaking condition, spilling, and plunging are defined according to a previous study of Rapp et al. (1990).

The numerical domain is discretized using a 6345 × 443 rectangular mesh considered for the simulations. The mesh domain is composed of the stretching zone and the uniform grid zone. The base mesh is refined three times to obtain a finer grid size of 0.001 m near the free surface. A constant cell size of 0.001 m is generated in the stretching zone of the length 2.0 m around the wave-focused area in the x-direction from 5.3 m to 7.3 m, so that it can cover both non-breaking, spiller, and plunger focusing location and propagation details. To reduce the effect of aspect ratio, the stretching grid around the wave focused area is kept as a square mesh with an aspect ratio of 1. The grid size in the uniform zone is 0.003 m. The stretching zone in the vertical direction is the same

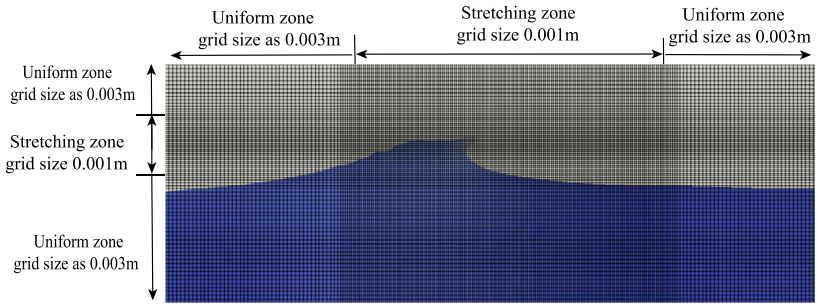

Fig. 2. Sketch of the numerical wave tank.

for all cases with uniform grid size 0.001 m from 0.465 m to 0.615 m. There is a short cross-zone between the stretching zone and the outside uniform grid zone. The distribution of the stretched grid near the free surface is illustrated in Fig. 2.

2.3. Focused wave generation

There are several physical mechanisms inducing wave breaking in experiment and simulation studies. Energy dispersion focusing, wind fetch, wave–current coupling, and modulational instability may all introduce wave breaking. In the simulation, the pre-determined energy-focused wave is generated based on the constant wave steepness method.

In this paper, linear superposition wave theory is adopted to generate focused waves. In the spirit of this method, the target focused wave are composed by individual sinusoidal harmonic waves with same wave steepness. The first-order focused wave theory is employed for the free surface defined as:

$$\eta^{(1)} = \sum_{i=1}^{N} A_i \cos(k_i x - \omega_i t - \psi_i), \tag{5}$$

where, A_i is the amplitude of ith wave component, k_i is the wavenumber, $\omega_i = 2\pi f_i$ is the radian frequency and ψ_i is the phase. ω_i and k_i follow the dispersive relation as follows:

$$\omega_i^2 = g k_i \tanh(k_i d) \tag{6}$$

where d is water depth.

The phase angle ψ_i is determined by setting $\cos(k_i x_f - w_i t_f - \psi_i) = 1$ with the preset focused time t_f and location x_f.

$$\psi_i = k_i x_f - \omega_i t_f + 2\pi n (n = 0, \pm 1, \pm 2, \ldots) \tag{7}$$

The wave amplitude of each wave component calculates in terms of the specified wave steepness:

$$A_i = \frac{S_t}{k_i} \tag{8}$$

where, S_t is the fixed wave steepness of each component and $S_t = \frac{\varepsilon}{N}$, $\varepsilon = N k_i A_i$ is the initial wave steepness of the target focused wave for the wave generation.

The velocity at the inlet boundary condition can be expressed in terms of the first-order focused wave theory and the linear superposition

$$u^{(1)} = \sum_{i=1}^{N} A_i \omega_i \frac{\cos h(k_i(z+d))}{\sin h(k_i d)} \cos\theta_i \tag{9}$$

$$w^{(1)} = \sum_{i=1}^{N} A_i \omega_i \frac{\sin h(k_i(z+d))}{\sin h(k_i d)} \sin\theta_i \tag{10}$$

Table 1
The classification of water depth in wave analysis.

Water depth	Shallow water	Intermediate water	Deep water
	$d/L_w < 1/20$	$1/20 < d/L_w < 1/2$	$d/L_w > 1/2$

d is the water depth, L_w the wave length.

2.4. Initial and boundary conditions

The relaxation zone method is employed for wave generation and absorption numerical beach for better wave quality and due to the better absorption of the wave at the end of tank and very little reflection Mayer et al. (1998) and Jacobsen et al. (2012). The analytical values of the velocities, free surface and pressure based on first-order wave theory are expressed by the relaxation function in the relaxation zone for wave generation. At the outlet boundary, the numerical beach-another relaxation zone is set to absorb the incident waves and prevent unwanted reflections.

$$F(\widetilde{x})_{analytical} = \Gamma(\widetilde{x}) F_{theoretical} + (1 - \Gamma(\widetilde{x})) F_{computational} \tag{11}$$

where $F(x)$ can represent velocities, free surface evolution and pressure at each point $\widetilde{x}$ of the relaxation zone and $\widetilde{x}$ is scaled to the length of the relaxation zone. The length of the relaxation zone is usually taken with one wavelength. For the numerical beach, the relaxation method is employed in all cases with around two wavelengths. The relaxation function in the relaxation zone and numerical beach used is expressed as follows:

$$\Gamma(\widetilde{x}) = 1 - \frac{e^{(\widetilde{x}^{3.5})} - 1}{e - 1} \quad for\ \widetilde{x} \in [0; 1] \tag{12}$$

The top and two side boundaries of the computational domain are treated as symmetry plane where the free slip mixed boundary condition is applied. The bottom of the NWT is regarded as a rigid wall and the law of the wall is applied.

At $t = 0$s, the wave tank is initialized with $u_i = 0$ for both the air and water phases and the free surface keeps $z = 0$. The pressure distribution in the whole domain is hydrostatic. The level set function is reinitialized after each time step to maintain its signed distance property and to ensure mass conservation.

2.5. Breaking criteria

Three typical breaking criteria are introduced in this section, including a. Geometric criterion, b. kinematic criterion, and c. Dynamic criterion. These three criteria are estimated based on the simulated wave profile and their performance in predicting wave breaking are described by the variation tendency between the corresponding predictional parameter and the increasing wave steepness. The breaking criteria studied in this paper are specified and adopted in finite water depth. The classification and definition of water depth over which the oscillation propagates have been summarized in Table 1.

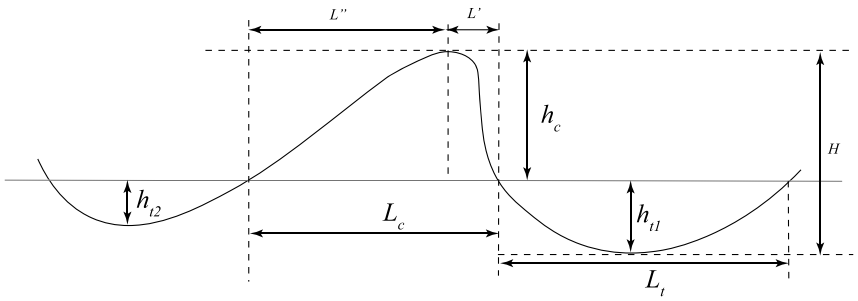

Fig. 3. Definition sketch of wave geometric parameters for focused extreme waves.

2.5.1. Geometric criterion

(1) Theoretical wave breaking criterion

Based on the connection between wave height H and wave period-related parameter gT^2, Ramberg and Griffin (1987) presents that the ratio between these two parameters can be a breaking criterion. This ratio usually was compared with theoretical limiting wave height $H = 0.027gT^2$, which is calculated based on the Stokes limiting wavelength and second-order relation between wavelength and period $L = 1.2gT^2$. Fig. 3 gives a concise definition of wave geometry parameters used in this paper.

(2) Global wave steepness

In this study, we adopt the global wave steepness ϵ for the sake of consistency with our focused wave generation method. The linear superimposed of the steepness of all the components is expressed as $\epsilon = NA_ik_i$ and each wave component has the same wave steepness. Here, N is the total wave components number, k_i is the wavenumber of ith component given by the linear dispersion relation and A_i is the wave amplitude of each wave component.

(3) Local wave geometric steepness and asymmetry

There are many geometry parameters to describe the wave geometric steepness. In the experiment of Rapp et al. (1990), they used two parameters, the wave crest steepness $\alpha = h_c/L'$ and the measured local steepness H/L to investigate the effect of bandwidth on wave breaking with low carrier steepness. From their results, it is insufficient to use the wave geometric parameters during the focusing onset process to estimate the type of breakers, however, the derivation of steepness can be a good predictable criterion. Wu and Nepf (2002) introduced local steepness and asymmetry using four typical geometric parameters, (a) the crest front steepness $\alpha = h_c/L'$ similar with the wave crest steepness in Rapp's paper (Rapp et al., 1990), (b) the crest near steepness $\delta = h_f/L''$, (c) the vertical asymmetry $\psi = L''/L'$, (d) the horizontal asymmetry $\mu = h_c/H$. Tian et al. (2010) adopted an another definition of local wave steepness $\epsilon_b = k_b\sum a_n$. They pointed out that the local wave steepness is strongly related to the energy dissipation rate. From the above studies, we conclude that it is essential to compare and find a better indicator to predict the onset of wave breaking. Finally, the local geometry parameters are taken into consideration and their sensitiveness with regard to characterizing breaking onset is analysis. These geometry parameters are measured at the incipient time section just before the wave breaking. As to the instability of the breaking process, the incipient scenario is chosen when the wave crest front almost become vertical as shown in Fig. 4.

2.5.2. Kinematic breaking criterion

The ratio of the maximum horizontal particle velocity $|\vec{U}|$ and the local phase speed of the crest propagation is the kinematic breaking indicator. The breaking wave was predicted when $|\vec{U}|/C_p \geq 1$ (Longuet-Higgins, 1969). The kinematic criterion analysis includes the determination of two parameters, maximum horizontal water particle velocity and the local wave phase speed.

$$|\vec{U}| = [u^2 + v^2]^{1/2}, \tag{13}$$

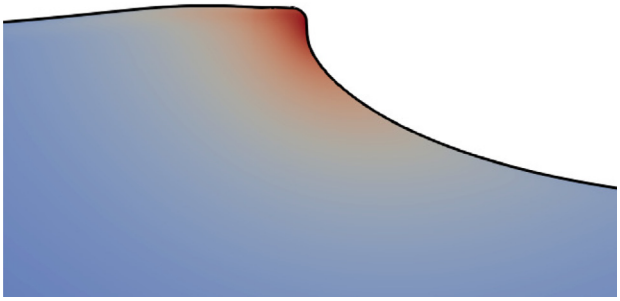

Fig. 4. Sketch of steep wave incipient section wave crest.

where u is the particle velocity component along in the x-direction and v is the component transverse in the y-direction.

A linear dispersion assumption is used for an acceptable estimation of the wave phase speed. From the above studies, we adopt the local wave speed definition as follows in Eq. (14) to calculate local phase speed C_p.

$$C_p = \frac{\omega_b}{|k_b|}, \tag{14}$$

The local angular frequency is calculated by $\omega_b = 2\pi/T_{tt}$, where T_{tt} is the time between two troughs around the crest of the wave gauge at the real focused position. For the local wavenumber k_b is computed from the local wave crest length defined in Fig. 3, $k_b = \pi/L_c$. The incipient moment when the front crest is vertical to the free surface is selected to calculate the local wave number k_b.

2.5.3. Dynamics breaking criterion

As for the analysis above, we adopt the energy dissipation rate as the dynamic breaking criterion parameter.

Following the energy analysis of Tian et al. (2010), the total energy is estimated based on the wave elevation measurements at fixed spatial locations. The linear theory energy flux is used to estimate the total energy as follows:

$$E(x) = \sum_{t=1}^{N} \rho g C_{gs}\eta^2(x,t), \tag{15}$$

where $\eta(x,t)$ is the surface elevation recorded by wave gauges and C_{gs} is the spectrally weighted group velocity estimated from the wave elevation defined by Drazen et al. (2008) as:

$$C_{gs} = \frac{\sum\left(C_{gn}a_n^2\right)(\Delta f)_n}{\sum\left(a_n^2\right)(\Delta f)_n} \tag{16}$$

A_n and C_{gn} are the wave amplitude and linear group velocity of each wave component of the wave group, respectively. The group velocity C_{gn} was measured by tracking the wave group maximum. Several wave gauges are probed to measure the surface elevation to evaluate the group envelope and the maxima. Δf is the constant frequency difference between wave components.

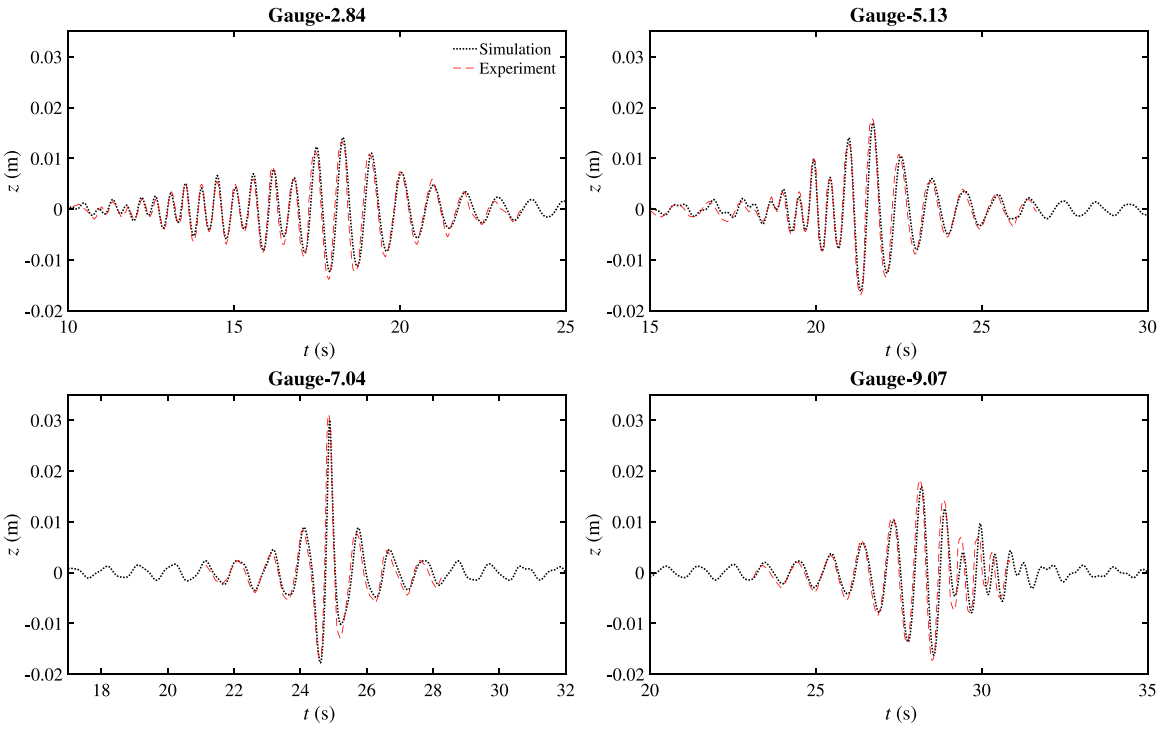

Fig. 5. Comparison of the computational and experimental results of the wave elevation at four gauges for Nonbreaking wave case DF1. Black dotted lines are present numerical results and red dash line are the experimental data.

Based on the previous studies, a parameter to describe the wave energy variation rate is proposed to investigate the energy dissipation and the relations between wave breaking. The energy changing rates of focus and dissipation process are both estimated within a local wavelength $L_b = 2L_c$, L_c is the distance between two adjacent zero-crossing points defined in Fig. 3. The energy variation rate is calculated as follows:

$$R = \frac{\Delta E}{L_b} C_p, \tag{17}$$

where ΔE is the energy variation values within a local wavelength L_c, this parameter can be assigned as ΔE_f and ΔE_d corresponding to the focusing and dissipation process separately. The local wave phase speed C_p calculated using Eq. (14).

3. Results and discussion

In this section, we present the comparison of the wave elevation both for non-breaking and breaking cases between the numerical and experimental results to verify and validate the present numerical wave tank model. Based on the validation research, the wave characteristics and three typical breaking criteria have been studied and analyzed.

3.1. Verification study

In this part, we provide verification of both focused non-breaking and breaking wave cases with experimental results.

The validation of the numerical model is proved by comparing the numerical free surface elevation and the experimental results of the focused nonbreaking case DF1 and breaking case DF2 at four wave gauges. Four wave gauges are located at the computational domain in Fig. 1. The computational results are compared with the experimental data captured by the high-speed imaging technology from the experiments carried out by Tian and Choi (2013). Wave gauge recorded 35s surface elevations for two cases, DF1 focused nonbreaking wave and DF2 focused plunging breaking wave case are shown in Figs. 5 and 6 separately. For the case of the nonbreaking waves, the wave elevation of the simulation results agree with the experimental data almost perfectly in Fig. 5. The numerical wave elevation for plunging breaking waves also has a good agreement with the experimental data in Fig. 6. The numerical results can replicate the wave elevation the same as the experimental results for both before and after breaking scenarios. Since the focused wave is a strong nonlinear phenomenon and very sensitive to the prescribed focused position and time, the good agreement of the wave elevation at different wave gauges along the wave tank indicates successful simulations of the focused breaking processes using the numerical model.

3.2. Wave characteristics analysis

In the above section, the numerical wave elevations agree with experimental results in different wave gauge for both non-breaking and breaking wave cases. The wave elevation has a abruptly rogue increasing around the focused position and shows irregular and nonlinear wave generation and propagation progress. Therefore, it is significant to further study and analyze the wave characteristics of the focused breaking waves. The purpose of this section is to analyze wave strong nonlinear profile, kinematic field and the process of energy focusing and dissipation during the progress of wave focusing and breaking with different wave steepness.

3.2.1. Strong nonlinear characteristics of breaking waves

The strong nonlinear profiles of the focused breaking waves were not only performed by local geometric parameters but also indicated by the difference between the setting focused position x_f and time section t_f and real focused position x'_f and time instant t'_f. The differences between the presetting focused position as well as time and real results are defined as X_{rf} and T_{rf}. The variation of X_{rf} and T_{rf} versus the increase of global wave steepness is shown in Fig. 7. The variation of focused positions can be roughly approximated as a piecewise function having a linear monotonic profile of each segmentation. The abruptly shifted variation values of the second demarcation point with ε ranging 0.6–0.65 is larger than that of the first shift with ε changing 0.3 to 0.35.

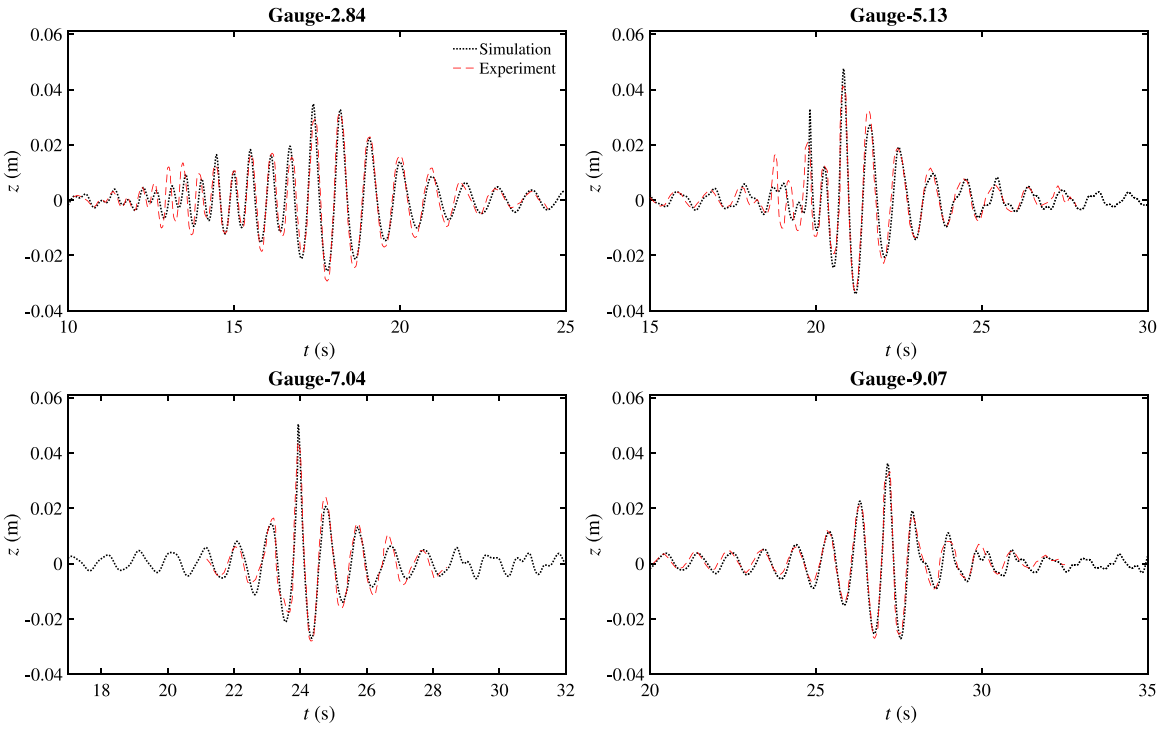

Fig. 6. Comparison of the computational and experimental wave elevation at four gauges for Breaking wave case DF2. Black dotted lines are present numerical results and red dash line are the experimental data.

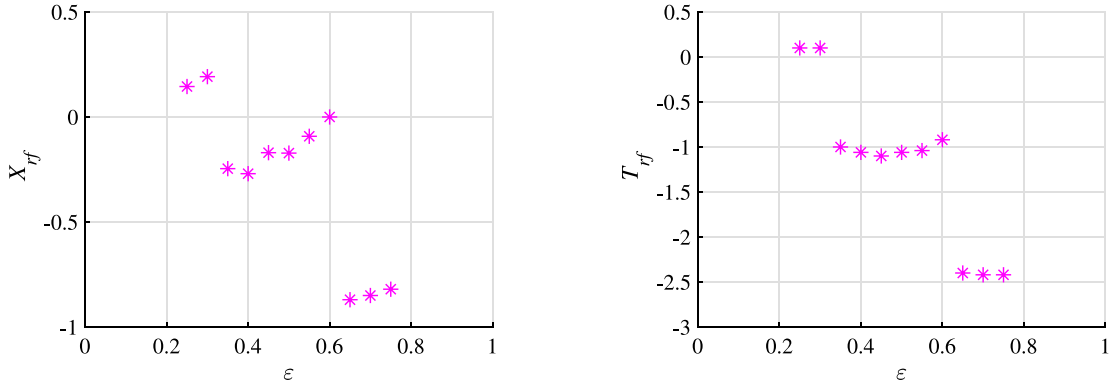

(a) Relations between gloabl wave steepness, ε and difference of real and prescribed focusing location, X_{rf}.

(b) Relations between global wave steepness ε and difference of real and prescribed focusing time, T_{rf}

Fig. 7. Relations between global wave steepness and difference of real and prescribed focusing location and time.

For the first segmentation, the focused position moved downstream as a linear trend from the setting position and shifted upstream abruptly at 0.35 global steepness. The second and third demarcations follow this changing trend and the focused position moved downstream relative to the shifted demarcation point. It is proved that the position of wave energy-focusing varies nonlinearly when the input focused position keeps as a fixed value. Rapp (Rapp et al., 1990) also analyzed the changing of the focused position in their study and had similar results with our study. Compared with the changing of the focused position, the real focused time in Fig. 7(b) almost follows the changing trend of the focused position in Fig. 7(a). Different from the linear changing after abrupt shifts of the focused position, the focused time almost keeps constant after the demarcation point. The abrupt shift of time and position is related to the energy changing during the focused process and it is revealed by the wave surface elevation of the focused waves in Fig. 8.

The color curves in Fig. 8 are the wave surface elevation with different time sections. The time interval for the wave surface capture is 0.02 s. Wave surface elevations are plotted by connecting surface points recorded with a constant distance interval as 0.003 m in x-direction. The black dotted lines in each figure respect the wave surface elevation at the focused section. The wave surface elevations of the all-time section are composed of the wave envelope, which has a fair external contour. The existence of the wave packet also suggests the quantities and position of energy and amplitude focused. In Fig. 8 the wave focused with the swell wave packet. Several swell wave packets with relative lower amplitude near the focused wave packet where have the maximum wave amplitude. From Figs. 8(a) to 8(b) the focused position moved from the middle wave packet to the position of the first wave packet, which also corresponds to the first demarcation where the focused position shifted abruptly. The focused wave keeps at first wave packet even for global steepness as 0.4 and 0.45 in Figs. 8(c) and

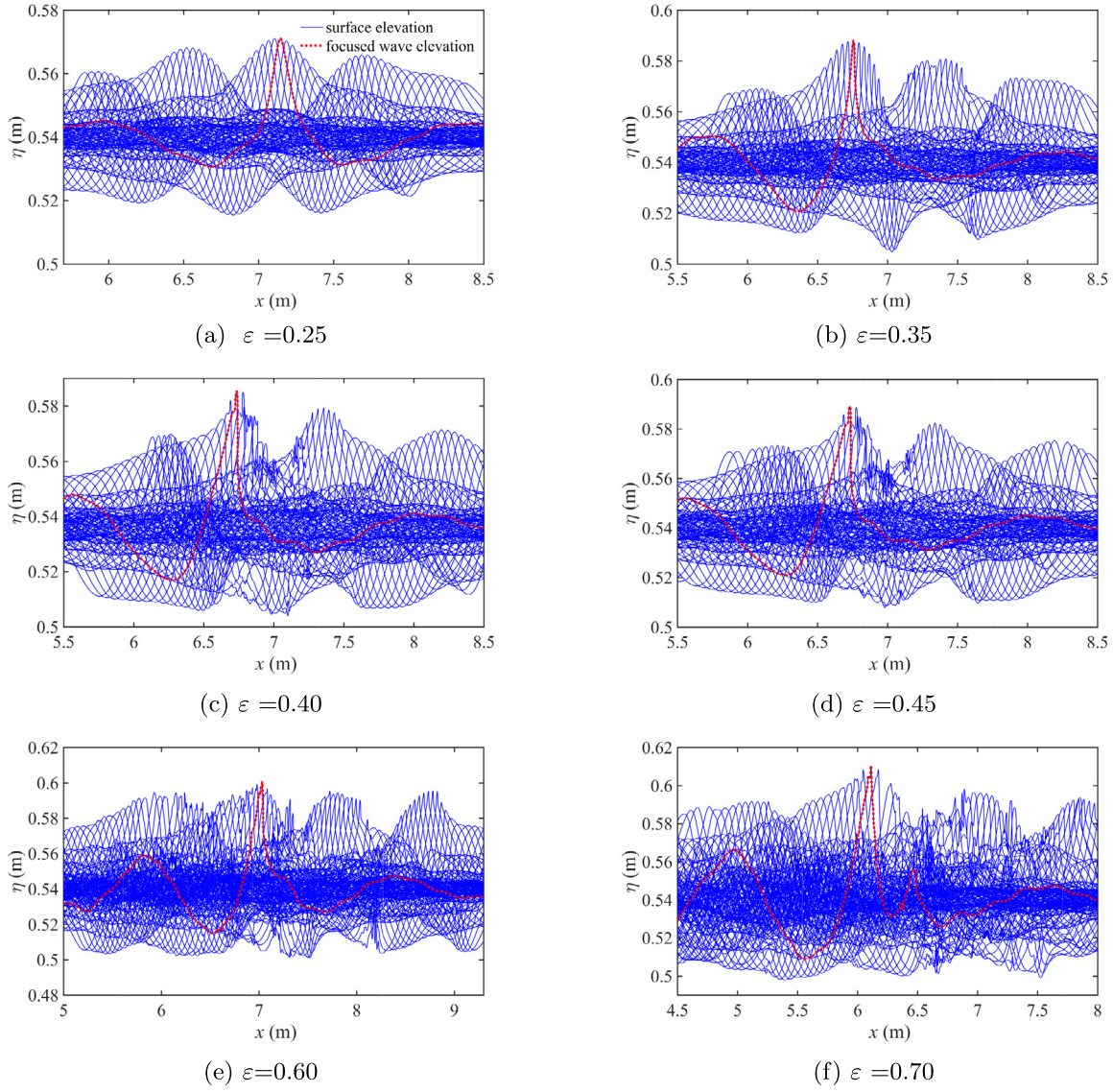

Fig. 8. Wave surface elevations of each time intervals for several cases. (a) ε = 0.25, (b) ε = 0.35, (c) ε = 0.40, (d) ε = 0.45, (e) ε = 0.60, (f) ε = 0.70.

8(d), corresponding to spilling and plunging breaker separately. As the increase of the global wave steepness, the amplitude increases not only for the focused wave packet but also wave packets near it. In Fig. 8(e) the difference of the amplitude between the neighbor wave packet and the focused packet is very smaller with the global steepness of 0.6. It also proves the energy and amplitude increase of the wave packet near the focused wave packet. The focused wave packet in Fig. 8(e) and the upstream wave packet combine with each other and form a new wave packet with higher amplitude when the global steepness rises to 0.7. This suggests that the energy and amplitude of the focused wave packet and the neighbor packet rise at the same time with the increase of global wave steepness. When the amplitude of the neighbor packet is near the value of the focused wave packet, the focused position will have an abrupt shift as the increase of steepness and input energy. So it can be summarized that the changing of the focused position is due to the energy focusing and distribution mechanism. The energy focusing process also has a strong nonlinear profile.

The overturning process is another typical strong nonlinear phenomenon. For the plunging breaking wave, the overturning jet brings an entrained air cavity during the process of first curling and splash-up. New (1983) proposed an applied mathematical model to describe the front crest overturning phenomenon. A certain region of the front surface beneath the overturning crest can be well approximated by an ellipse. Based on this indication, the more wave develops, the more accuracy the underside cavity of the breaking crest becomes to a $\sqrt{3}$-aspect-ratio ellipses. Bonmarin (1989) did a comparison between their experimental results and New (1983) mathematical solution, and got a good agreement. To analyze the variation of air cavity beneath the first splash-up overturning jet, the scenario shown in Fig. 9 when the first overturning jet penetrates into the free surface is selected to calculate the area of the best-fitted ellipses on these observed profiles. The selected ellipse satisfied the requirement of along the largest portion underneath the overturning jet A successive approximation determines an accuracy fitness, so the axes ratio of the fitness ellipse in Fig. 9 is around $\sqrt{3}$ in the theory of New (1983).

The area of the air cavity denoted as A_e beneath the overturning jet versus the global steepness is shown in Fig. 10. The area of the air cavity is roughly a linear function of global steepness ε. For our wave groups, it is found that $A_e = 5.35\varepsilon$. This indicates that wave groups of relatively large wave steepness increase in the area of the air cavity beneath the overturning front jet. More area of air cavity means more strong mixing of the air and water after breaking of large wave steepness. An increase of the front cavity reflects the wave falling crest height of breaking waves rises. The area of the air cavity can also

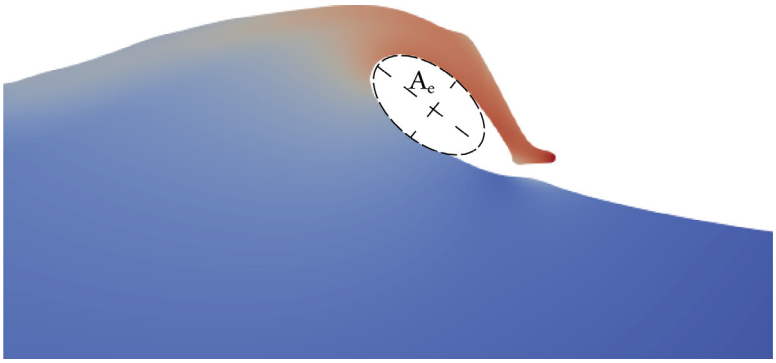

Fig. 9. Sketch of the best-fitted ellipses at the scenario of first impingement.

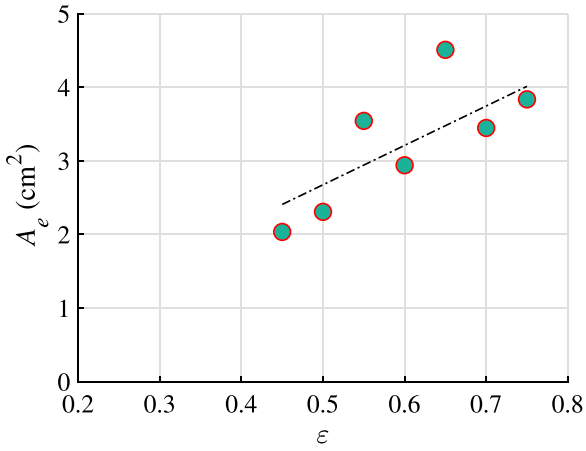

Fig. 10. Correlation between area of the best-fitted ellipses of the air cavity A_e and global wave steepness ε. The solid line represents a linear least-squares fit and the slope is 5.35.

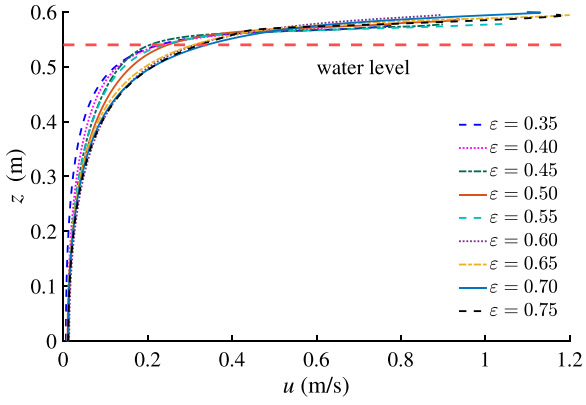

Fig. 11. Horizontal velocity profile below wave crest.

be a rough indicator to calculate and analyze the air-entrainment and air–water mixing intensity after wave breaking.

3.2.2. Velocity field analysis

The vertical velocity fields beneath the crest surface at the incipient scenario are shown in Fig. 11. The velocity rises exponentially in the vertical direction and has maximum values at the wave crest. The curvature of velocity distributions for different global wave steepness is different from each other. Waves with larger steepness correspond to having a more curving velocity distribution. From this distribution, the maximum velocity exists around the wave crest, so the maximum horizontal velocity is picked up near the crest for kinematic criterion analysis.

Fig. 12 shows the evolution of the horizontal velocity field of the spilling breaking process. The velocity is an oriented arrow to the direction of particle velocity and is scaled by the values of horizontal velocity. Four typical breaking scenario is selected and shown in Fig. 12. The green dots in each figure is the location of the maximum velocity of the present time section. The position of the green dot is always located at the top of the crest or the front of the ejecting jet, which indicates that the location of the maximum velocity occurs. The incipient scenario when the crest front surface is vertical relative to the water level is shown in Fig. 12(a). Local maximum velocity is $U_{max} = 0.86C_p$ at the incipient section in Fig. 12(a). The particle velocity at the crest exceeds the front wave surface and backward wave face, which will compress the front wave face and stretch the backward wave face, resulting in a breaking jet in Fig. 12(b). Compared with the plunging breaking wave with a large plunging tongue at the front crest jet, the spilling breakers show a smaller ejecting jet at the top of the crest in Fig. 12(b). The maximum velocity occurs at the splash-up section in Fig. 12(c) of the entire spilling breaker process with a magnitude of $1.2C_p$. After a weak splash-up, the crest jet falls to the front surface mixing with entrainment air and swells forward in Fig. 12(d). After splash-up, the values of maximum velocity decrease apparently and the water surface pushed upward.

Velocity fields of the plunging breaking wave are depicted in Fig. 13. The maximum velocity at the incipient section in Fig. 13(a) is $U_m = 0.936C_p$, which is larger than that for spilling breakers. A large air cavity is generated by the first rolling continuing to curl and moving forward. The maximum velocity particle is located at the plunging tongue for the entire overturning process such as the scenario in Fig. 13(b). After the fully rolling and development, the overturning water jet falls and impinges on the front wave trough surface in Fig. 13(c). The scenario in Fig. 13(c) is defined as 'impingement' and has maximum local velocity along this plunging breaking process as $U_{max} = 1.31C_p$. A splash-up is generated by the strong impingement of the falling jets in Fig. 13(d) and the maximum velocity at this moment is smaller than that in the impingement scenario in Fig. 13(c). The maximum of the horizontal particle velocity increases when the splash-up developed as second clockwise rolling in Fig. 13(e). The maximum particle velocity arrived $U_{max} = 1.18C_p$ just below the values of impingement moment. A backward counterclockwise rolling is generated and develops as a negative impingement between the first clockwise impingement and the second rolling in Fig. 13(f). This phenomenon is also captured by Lim et al. (2015) and defined as backward impingement in their research. An air cavity generated by first penetrating rolling exists under the free surface. Two clockwise and one backward impingement formed an irregular triangular packet, which was called as surface zone and ascending crest of the breaking waves in Lim et al. (2015) and Nadaoka et al. (1989). After these overturning and mixing of the plunging breakers, the focused wave

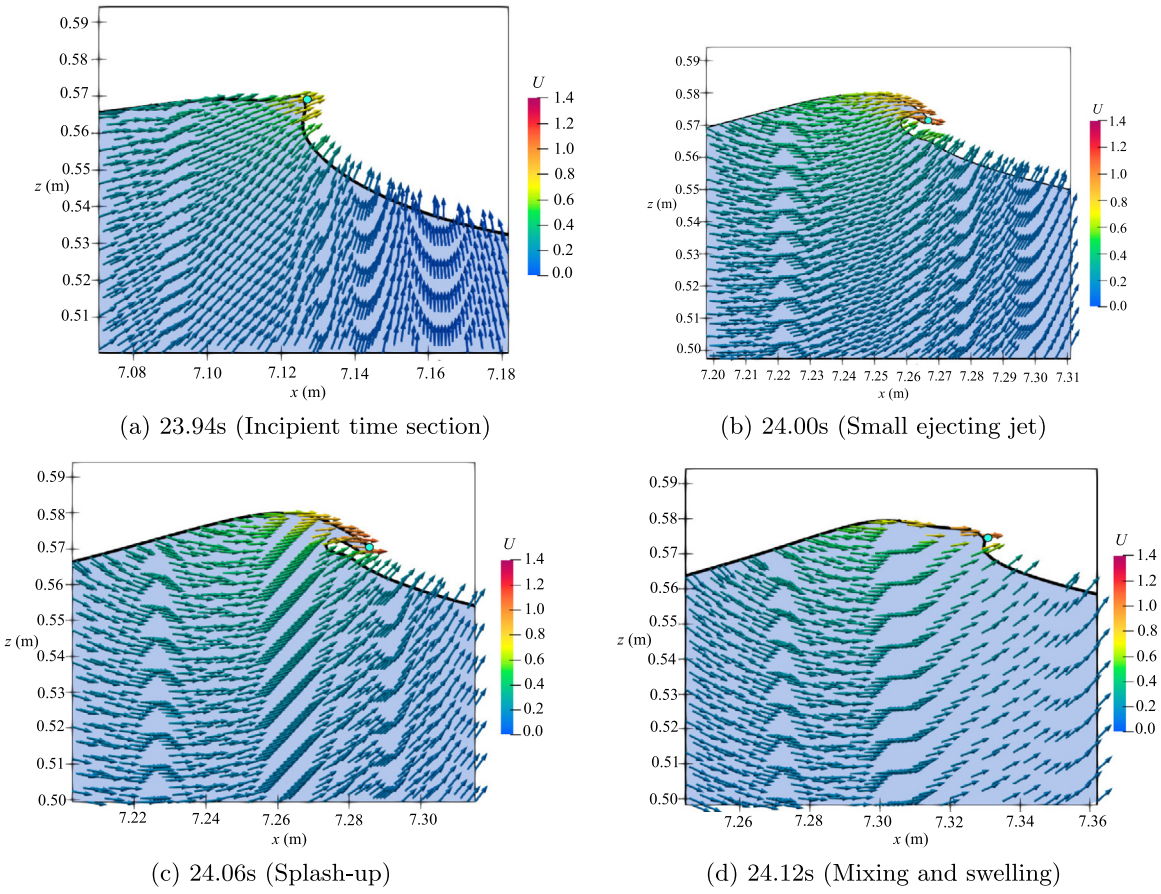

Fig. 12. Velocity field of focused wave breaking process for case WG2 with $\epsilon = 0.40$. a. 23.94 s (incipient section), b. 24.00 s (first overturning), c. 24.06 s (first impingement), d. 24.12 s (spilling breaking).

energy dissipates and the maximum velocity decreases apparently at this moment. The variation of the maximum horizontal velocity for different global wave steepness is introduced in Fig. 20. It will have more detail and direct understanding of the Umax changing during the entire breaking process.

3.2.3. *Qualitative description of breaking process and turbulence structure*

The profile of the vorticity distribution is very similar to the turbulence intensity (Lim et al., 2015). Fig. 14 shows the evolution of vorticity and turbulence structures distributions during strong plunging breakers for global steepness 0.7. With the free surface as boundaries, the turbulent structures on both air and water are displayed contoured by the magnitude of the vorticity field. The motion of the free surface generates chaotic turbulent structures around the free surface in both air and water phases. Concentrate negative vorticities existed above the breaking crest in the air phase at each breaking moment selected in Fig. 14. At the incipient moment in Fig. 14(a) two pairs of vorticities locate at the front trough and stretch backward surface separately in the air phase. As the forward motion of the breaking crest, the vorticities existing in pairs at the backward of the breaking crest have a negative rolling over around the surface from the incipient moment 22.4 s to 23.04 s in Fig. 14(h). The vorticities existing in pair at the front trough in Fig. 14(a) always keep a distance of the wave surface and move from the front of the breaking crest to the back as the breaking wave propagates.

Before the incipient moment in Fig. 14(a) the vorticity field is almost irrotational beneath the wave surface, which is similar to the laboratory results of Perlin et al. (1996). As the development of the breaking crest overturning and plunging forward in Fig. 14(b), a relatively larger positive vorticity field is generated below the rolling crest and has a maximum value at the turning point of the splash-up cycle. After the first overturning crest penetrating into the wavefront surface, the potential energy has been transformed into kinematic and turbulent energy. This energy transformation not only gets an increase of the horizontal particle velocity but also leads to the formation of large vortices under the wave surface in Fig. 14(c). The energy dissipation due to wave breaking is the source of the energy for turbulent mixing around the wave surface and air entrainment. These energy transformations adjust the air–water energy exchanging and enhance the vortex propagation underwater. Air is entrapped into wave surface and the air entrainment phenomenon has been generated. Another splash-up is also generated and has maximum vorticities after the energy transformation. As the effect of inertial force, the first plunging impingement continues to roll forward and downward arousing a rising water volume between the entrapped air and second plunging jet in Fig. 14(e). The negative rolling generated between the first air–water mixing clouds and second rolling in Fig. 14(e) is defined as first negative rolling. This negative vorticity has been developed when the second plunging jet penetrated into the front surface and generated another air entrapped in Fig. 14(f). After the negative rolling impinging into backward and combining with the first air entrapped, collapsed bubble clouds and chaotic mixing vortex fields are generated in Fig. 14(g). The second negative vorticity develops between the third positive rolling and second air entrainment in Fig. 14(g). The third splash-up rolling and spilling forward dissipates the last energy of the breaking waves in Fig. 14(h). The turbulence intensity of this mixing air–water clouds flow decreases with the development of the breaking process and the wave surface tend to smooth after these breaking processes in Fig. 14. At the same time, the vorticity field has a more chaotic and complex profile. The complex clockwise and

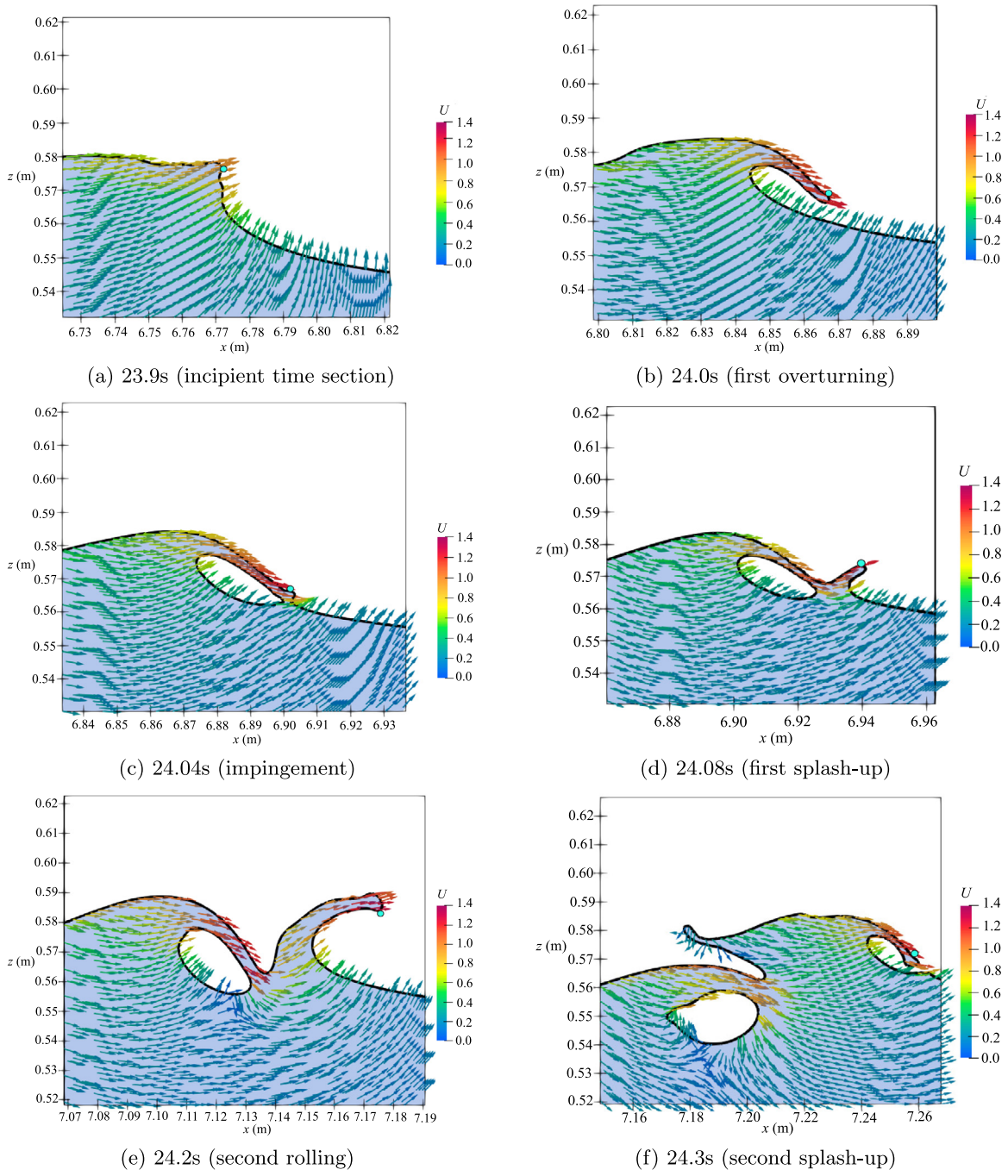

Fig. 13. Velocity field of focused wave breaking process for case WG4 with $\varepsilon = 0.45$. a. 23.9 s (incipient section), b. 24 s (first overturning), c. 24.04 s (first impingement), d. 24.08 s (first splash-up), e. 24.2 s (second rolling), f. 24.3 s (second splash-up).

counterclockwise vorticities generated during the breaking process are the main sources of turbulent kinematic energy dissipation.

3.3. Breaking criteria

The above analysis of wave characteristics give an insight view of focused breaking waves. Besides, the prediction of the onset of wave breaking is another crucial point for the understanding of wave breaking. In the present section, we adopted three typical breaking criteria to predict the focused wave breaking onset under infinite water depth.

3.3.1. Geometric breaking criterion

a. Stokes breaking limitation

The Stokes theoretical breaking limiting as the typical breaking criterion is analyzed in this section. The relations between wave height H and the period parameter gT^2 of the present results are shown in Fig. 15. The present limiting wave steepness at breaking inception is less than the Stokes limitation $H = 0.027gT^2$, which is consistent with the previous studies conducted by Duncan and Longuet-Higgins (1981) and Bonmarin (1989) in Fig. 15. As for the analysis of breaking criterion, it should be noted here that despite the different generation methods of the breaking waves, plunger and spilling breakers appear to have qualitatively similar properties.

Bonmarin also pointed out that the breaking coefficient $\sigma = H/gT^2$ depends on the breaker type. Although the highest values may be typically associated with plunging breakers, the author does not think

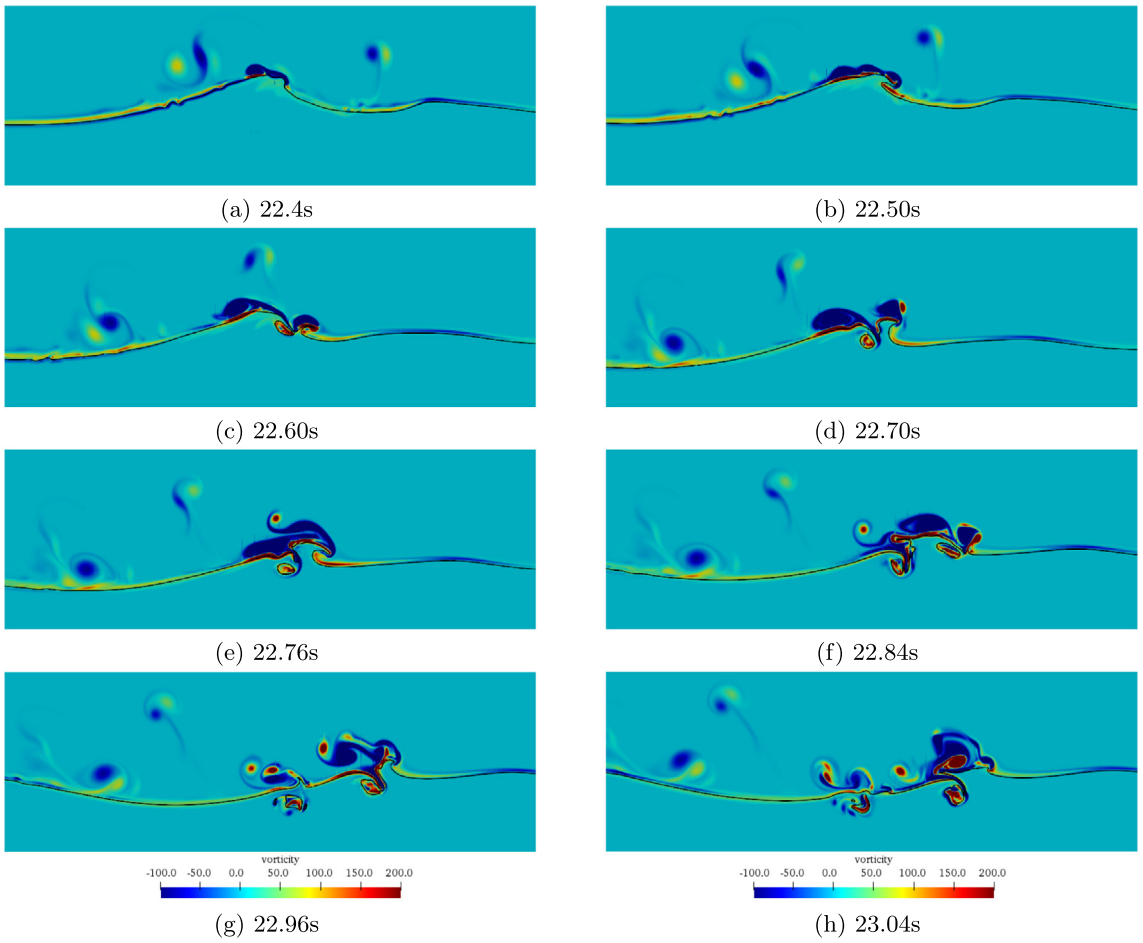

Fig. 14. Evolution of vorticity in both air and water during plunging breaking wave with global steepness $\varepsilon = 0.70$ WG9.

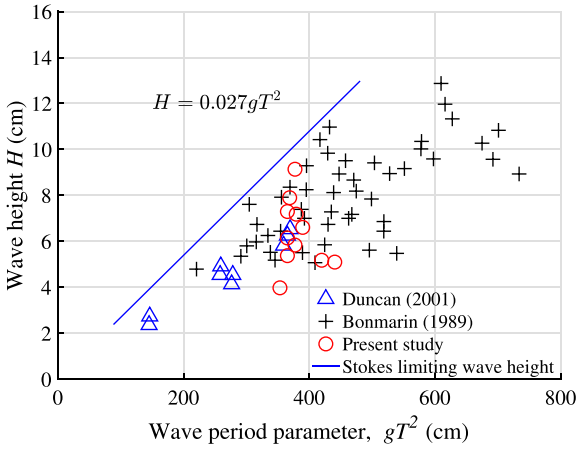

Fig. 15. Comparison of present results of wave amplitude H versus gT^2 with theoretical breaking criterion.

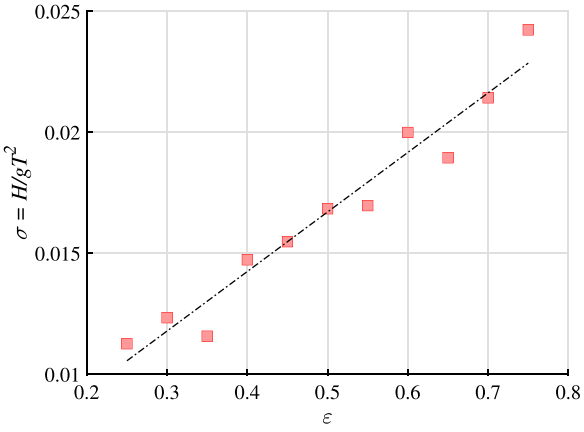

Fig. 16. Correlation between the breaking coefficient $\sigma = H/gT^2$ and global wave steepness ε. The solid line represents a linear least-squares fit and the slope is 0.0246.

the correlation is sufficient to mark the coefficient as a breaker classification parameter. As for the assumption and foundation, the relations between the breaking coefficient and global steepness are shown in Fig. 16. The present results show clearly a linear function trend between breaking coefficient σ and global steepness ε. As for the simulation results in this study, it is spilling breakers when global wave steepness is 0.4 and plungers for 0.45 global steepness. So in Fig. 16, the value of σ as 0.015 could be a classification threshold of the breaking type in this study. With the increase of the global steepness, the breaking coefficient will have a linear increase with the slope value of 0.0246. It is also consistent with Bonmarin's (Bonmarin, 1989) conclusion that higher values of breaking coefficient σ are, the rougher breaking waves are.

b. Global wave steepness

For focused waves, wave crest height as the typical wave geometric parameter reflects the amplitude focusing and the energy collection mechanism. For focused waves, when the wave crest reached a threshold value and arrived at the breaking criterion, a steep wave crest exists

Table 2
Comparison of the values of global wave steepness for predicting different breaking condition.

Breaking section	Lamarre	Chaplin	Kway et al. (1998)	Chin H. Wu 2-D	Chin H. Wu 3-D	Present simulation
Incipient	0.35	0.3		0.32	0.21	0.35
Spilling	0.40		0.59	0.40	0.26	0.40
Plunging	0.45		0.73	0.50	0.47	0.45

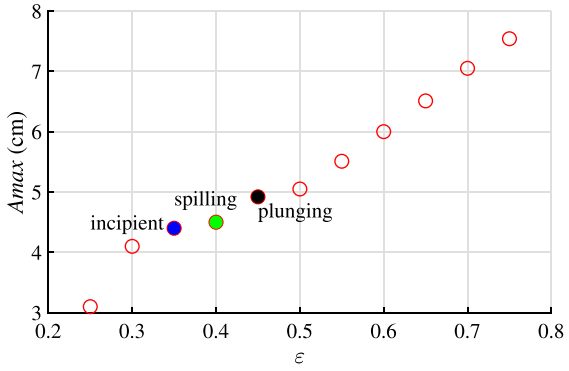

Fig. 17. Maximum wave amplitude changing along different wave steepness.

Table 3
Summary of wave geometric parameters.

Case	ε	Breaking type	k_b	$A_{max}(m)$	ε_b	C_p	$x'_f(m)$	$T'_f(s)$	$L_c(m)$
DF1	0.25	*N*	11.17	0.031	0.347	0.937	7.145	25.1	0.281
DF2	0.57	P	10.12	0.053	0.521	1.012	6.25	23.55	0.314
WG1	0.30	*N*	9.41	0.041	0.385	1.021	7.192	25.1	0.334
WG2	0.35	I	9.01	0.044	0.395	1.046	6.754	24.0	0.350
WG3	0.40	S	10.82	0.045	0.487	0.952	6.73	23.94	0.290
WG4	0.45	P	10.47	0.049	0.515	0.968	6.83	23.90	0.30
WG5	0.50	P	10.82	0.051	0.546	0.952	6.828	23.94	0.291
WG6	0.55	P	9.24	0.055	0.509	1.031	6.91	23.96	0.340
WG7	0.60	P	9.98	0.06	0.600	1.109	7.0	24.08	0.394
WG8	0.65	P	10.42	0.065	0.678	0.971	6.13	22.60	0.302
WG9	0.70	P	10.7	0.071	0.755	0.957	6.15	22.58	0.293
WG10	0.75	P	10.2	0.075	0.769	1.015	6.18	22.58	0.329

and breaking takes place. The maximum amplitude of the focused wave A_{max} along the increased global wave steepness is shown in Fig. 17. The primary wave parameters and breaking classification information are summarized in Table 3, spilling breakers (S) occur when global wave steepness reached 0.4 and plunging breakers (P) happen with 0.45 steepness. 'N' respects the nonbreaking profile and 'I' corresponds to the incipient section in Table 3. The corresponding focused and breaking profiles of each case have been marked in Fig. 17 for better understanding for the analysis of the geometric criterion parameter — global wave steepness. As the global steepness increases, the maximum wave amplitude shows a curve-increasing rate. After the focused wave arrived at the plunging profile, the increasing rate of the maximum amplitude show a linear trend. The focused waves generate different wave focus and breaking intensity as the increase of global steepness. It also indicates that the global steepness as a geometric criterion parameter can give a good prediction of the incipient and breaking section.

The comparison of the global wave steepness under different experiment settings and focused wave generation mechanics are collected and summarized in Table 2. The focused wave generated by the constant steepness spectra is selected. The wave steepness $a_i k_i$ is same for each wave component in Lamarre experiment (Lamarre, 1993), which is similar to the calculational method of the amplitude and frequency of each sinusoidal component in this simulation. The value of global wave steepness corresponding to different breaking sections and types are the same as the results of Lamarre (Lamarre, 1993). A higher threshold value of global steepness with the constant steepness spectra studied by Kway et al. (1998) under low frequency ranging from 0.56 Hz to 1.1 Hz. Compared with the values of this criterion under a relative high-frequency, wave energy with low frequency is more stable and has higher global wave steepness when generating breaking. Besides, it is also clear that this criterion is also influenced by the dimension and wave direction by comparing different dimensions results of Wu and Nepf (2002). This suggests that the wave energy distribution is not only related to the local wave energy collection in wave propagation direction but also has a relative amount of energy dissipating in three dimensions. Although the threshold of the global wave steepness have relative difference between different experiment and numerical studies, this criterion has a good prediction of wave breaking in each research. The influence of the setting wave parameter on the threshold values of this criterion still need further study and analysis.

c. Local wave steepness and asymmetry parameters

Fig. 18 shows the crest front steepness α, the crest rear steepness δ, the horizontal asymmetry factor ψ and the vertical asymmetry factor μ distribution versus the global wave steepness ε. It appears that these local geometric parameters increase for waves with larger global wave steepness. The distribution of the crest front steepness α shows a roughly linear trend along with the variation of global steepness in Fig. 18(a). The linear fitness of the front steepness α shows a good prediction of unique breaking incipient cases. For the simulation wave groups varying with different global wave steepness, the linear relation between α and ε fit $\alpha = 1.1665\varepsilon$. This implies that the focused wave of relatively large setting wave steepness has a more steep front crest. It also corresponds to the increased particle velocity and energy around the front crest of the breaking waves with large global steepness, which may change the amount of energy focusing and dissipation during the breaking process. It also indicates that the breaking process becomes more vigorous and has a strong irregular profile. Compared with the crest front steepness α, the crest rear steepness δ has a relatively smaller changing range and linear fitness slope 0.2335 versus ε in Fig. 18(b). Therefore, crest rear steepness is not a good indicator for predicting different wave breaking sections. In addition, the asymmetry parameter vertical factor ψ and the horizontal factor μ are insufficient to predict wave breaking as well as seen in Figs. 18(c) and 18(d).

The trend of the vertical asymmetry factor versus global wave steepness shows a relative discrete distribution compared to an increasing linear fitness. This suggests that the focused wave shows a relative focused axis symmetry profile before the incipient breaking section. Then the breaking wave generated by constant steepness-focused mechanism has a larger backward wave length L'' almost equaling to 2 times of front wave length L' with large wave steepness. This is an opposite phenomenon compared with the breaking waves induced by the decrease of water depth, which has been studied by Alagan Chella et al. (2015). In their study, the vertical asymmetry factor shows a decrease trend when the wave steepness factor H_0/L_0 becomes larger with a beginning values as 3.6 and ended with 2.1.

Besides these local steepness and asymmetry parameters, a local wave steepness $\varepsilon_b = k_b \sum a_n$ prior to wave breaking was introduced by Tian et al. (2010). A similar result with experiment of Tian et al. (2010) for a linear function between global wave steepness ε and local wave steepness ε_b has been achieved, shown in Fig. 19. The linear fitness function is $\varepsilon_b = 1.12\varepsilon$. Although the formula and geometric meaning of ε_b and crest front steepness α are different, the same

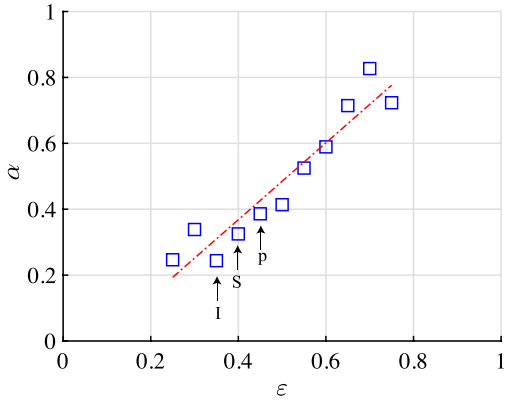

(a) Crest front steepness α versus global wave steepness ε. The dash line represents a linear least-squares fit: $\alpha = 1.1665\varepsilon$

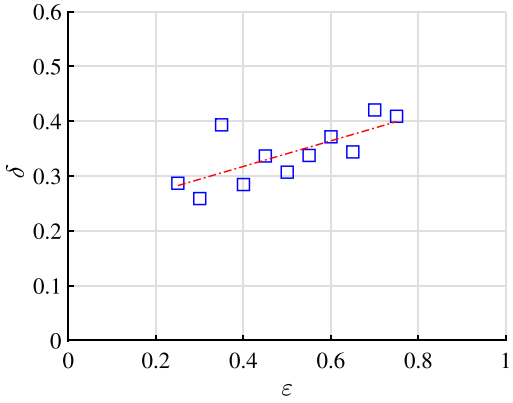

(b) Crest rear steepness δ versus global wave steepness ε. The dash line represents a linear least-squares fit: $\delta = 0.2335\varepsilon$

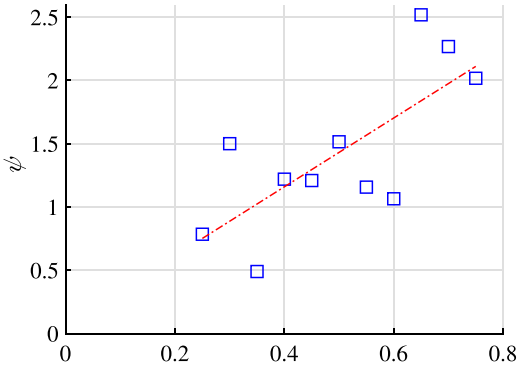

(c) Vertical asymmetry factor ψ versus global wave steepness ε. The dash line represents a linear least-squares fit: $\psi = 2.719\varepsilon$

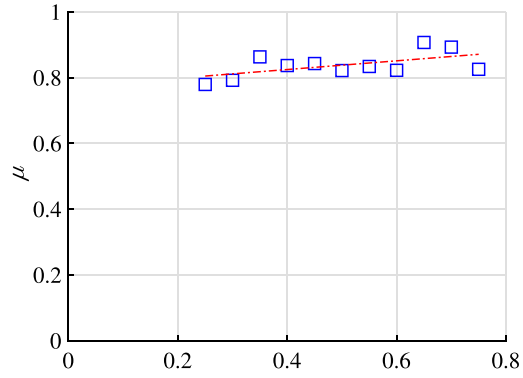

(d) Horizontal asymmetry factor μ versus global wave steepness ε. The dash line represents a linear least-squares fit: $\mu = 0.132\varepsilon$

Fig. 18. Local wave parameters versus global wave steepness ε.

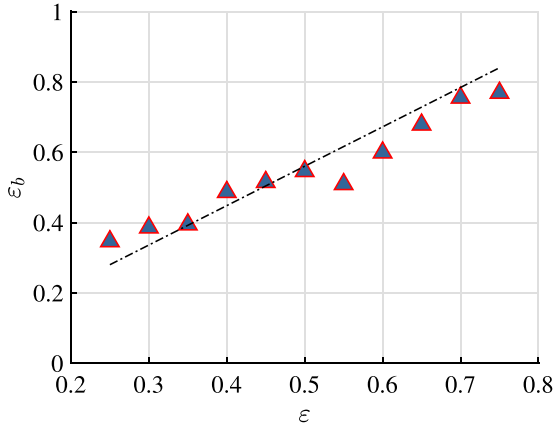

Fig. 19. Correlation between global wave steepness, ε and local wave steepness, ε_b. The solid line represents a linear least-squares fit: $\varepsilon_b = 1.12\varepsilon$.

indication that local wave steepness increase with large global wave steepness has arrived. It also proves the breaking crest can contain more energy and have a strong nonlinear profile with large global wave steepness. This factor also can be a good indicator to predict the unique wave breaking section.

3.3.2. *Kinematic breaking criterion*

The kinematic breaking criterion ratios $|\vec{U}|/C_p$ are calculated using Eqs. (9) and (13) and shown as blue solid lines in Fig. 20 for all cases with different global wave steepness. The typical kinematic breaking criterion $|\vec{U}|/C_p = 1$ as a threshold value is plotted as a dashed line. The time axis is initialized by the real focused time section T_f'. For the spilling and plunging breakers, the scenario for T_f' is selected when the front wave crest is vertical relative to the water level in Fig. 4. The maximum value of ratio $|\vec{U}|/C_p$ increase apparently for the nonbreaking waves with global wave steepness changing from 0.25 to 0.35. The kinematic energy rises and collects with the increase of global steepness. The maximum of the ratio $|\vec{U}|/C_p$ just below 1 for the incipient non-breaking case $WG2$ with $\varepsilon = 0.35$. The breaking phenomenon does not occur until $|\vec{U}|/C_p = 1$ when global steepness $\varepsilon = 0.40$ in Fig. 20. When $\varepsilon = 0.4$, a spilling breakers occurs, the ratio $|\vec{U}|/C_p$ only has one maximum amplitude values and a regular variation intervals above 1. When ε is 0.45, the interval above the threshold value has two extreme values, corresponding to the maximum particle velocity at impingement scenario and that at the second rolling section in Figs. 13(c) and 13(e) separately . It suggests that the velocity decrease apparently after the second rolling and impingement. The variation of the ratio of maximum particle velocity and local wave phase speed also provides another view of the kinematic energy changing during each breaking process.

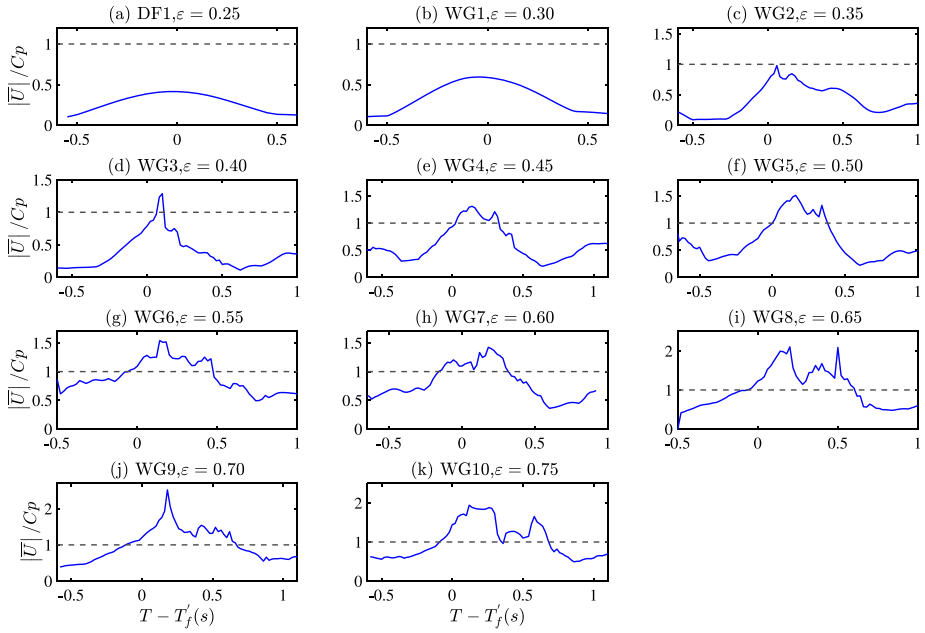

Fig. 20. Nondimensionalized instantaneous horizontal velocity (by C_p) under different wave condition along time.

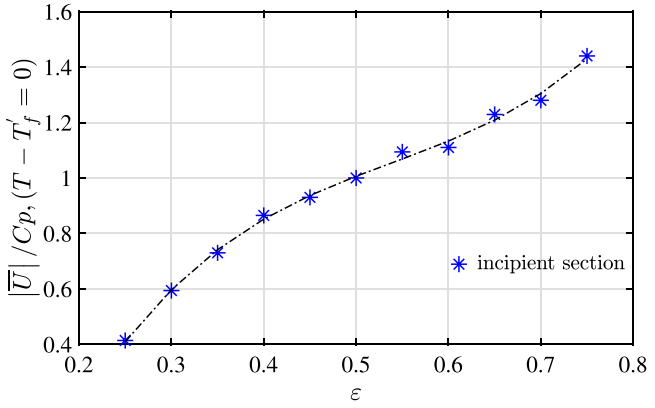

Fig. 21. Nondimensionalized instantaneous horizontal velocity (by C_p) with different wave steepness at incipient breaking section.

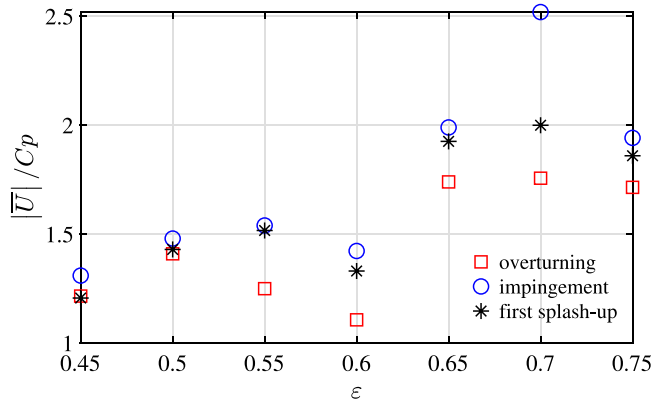

Fig. 22. Nondimensionalized instantaneous horizontal velocity (by C_p) with different wave steepness for three typical breaking section, overturning, impingement, and first splash-up.

The intervals when the ratio $|\vec{U}|/C_p$ above 1 for the spilling breaking process in Fig. 20d is shorter than that for plunging breakers with $\varepsilon = 0.45$ in Fig. 20e. This implies that the spilling breakers have a shorter breaking process compared with the plunging breakers. From the length of the time interval when the ratio $|\vec{U}|/C_p$ above 1 and ratio elevation exceeding the threshold value 1, The spilling and plunging breakers have an apparent difference between each other. So these two parameters may be an indicator to reveal the breaking type. The above phenomenons demonstrate that the kinematic breaking ratio not only predicts the breaking but also has functions to distinguish the variation of the breaking type and intensity. The kinematic breaking ratio $|\vec{U}|/C_p$ keeps a time interval with an oscillation variation when its values exceed 1 for cases $\varepsilon \geq 0.45$. These oscillations are related to the curling and penetrating phenomena during the breaking process. The kinematic breaking criterion satisfied $|\vec{U}|/C_p \geq 1$ for all breaking cases in this study. The kinematic breaking ratio $|\vec{U}|/C_p$ at the time section has different values for different global wave steepness in Fig. 20. This indicator gives a good prediction of wave breaking and reflects the breaking intensity from some characteristics.

The variation of the maximum particle velocity with the increase of global steepness ε at the incipient breaking moment is shown in Fig. 21. As the global wave steepness increases, the ratio $|\vec{U}|/C_p$ shows a nonlinear increasing tendency. This phenomenon has a similar conclusion in Stansell and MacFarlane (2002) that $|\vec{U}|/C_p > 1$ is not an essential requirement for wave breaking. It is found that the distribution of $|\vec{U}|/C_p$ versus ε satisfies a cubic polynomial curve-fitting. This implies a nonlinear relation between horizontal particle velocity and the global wave steepness. A focused wave group of relatively larger global wave steepness will have bigger horizontal particle velocity around the crest, which might lead to more violent wave breaking, thus resulting in more kinematic energy dissipation and rough breaking mixing around the free surface. The nonlinear relation also suggests that only using the values of $|\vec{U}|/C_p$ at a certain time section does not show a good prediction of wave breaking. However, the existence of the time interval when $|\vec{U}|/C_p$ shown in Fig. 20 can be a breaking criterion and the length of this interval is highly correlated with the breaking type and intensity.

As can be seen in Fig. 22, the maximum horizontal velocity occurs at the impingement moment when the breaking crest penetrates the wave

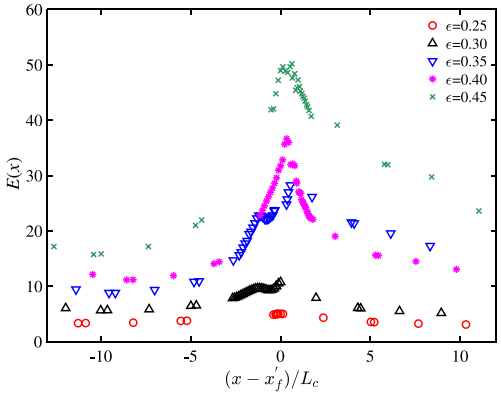

(a) Energy distribution along wave propagation direction for steepness range from 0.25 to 0.45

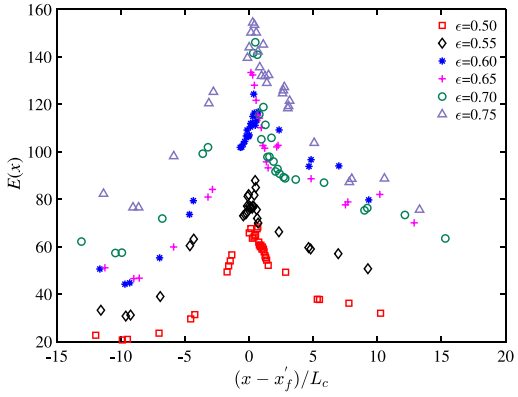

(b) Energy distribution along wave propagation direction for steepness range from 0.50 to 0.75

Fig. 23. Estimation of total energy distribution for all cases.

surface with a magnitude at a range from $1.3C_p$ to $2.5C_p$ as the increase of wave global steepness. After impingement of the overturning crest, there is a smaller decrease of the ratio $|\vec{U}|/C_p$ for the first splash-up moment beside the results when $\epsilon = 0.7$. It is also indicated that strong nonlinear kinematic energy dissipation occurs for larger global wave steepness. The ratio $|\vec{U}|/C_p$ during the breaking process after the incipient moment shows a rough separating chunk at $\epsilon = 0.6$ and the values of $|\vec{U}|/C_p$ show an abrupt increase no matter at which breaking moment. Global steepness as 0.6 is also a segmentation point for the focused position and time in Figs. 7(a) and 7(b). These phenomena prove that the velocity variation has the same abrupt shifting during the breaking as the increase of global wave steepness. The energy focusing mechanism is the basic reason for these strong nonlinear generations.

3.3.3. Energy dissipation analysis and dynamic criterion

Wave breaking inhibits wave propagation-reversal symmetry of focused nonbreaking waves (Alberello et al., 2018). It also means that the focused breaking waves have a distinct asymmetry profile of the focusing and defocusing processes. The asymmetric profile is not only reflected from the geometry characteristics but also exists on the energy focus and dissipation process. The evolution of total energy along wave tank has been shown in Fig. 23. The values in the x-direction have been normalized by the real focused position x'_f of each case and local crest wavelength L_c. The total energy has the maximum value when $(x - x'_f)/L_c = 0$. For a clear view of the total energy profile, the results of all cases have been separated and depicted in two figures in Fig. 23. The maximum values of the total energy $E(x)$ rise significantly as the increase of global wave steepness, which proves that the focused waves with larger wave steepness will collect more wave energy before breaking. Energy distribution of nonbreaking waves with steepness as 0.25 and 0.30 shows a relative symmetric profile taking the focused position as the symmetry axis in Fig. 23(a). When the global steepness is 0.35, the asymmetric profile of the focusing and defocusing process has been revealed. The overall change trends of total energy $E(x)$ on both sides of the focused position show asymmetric profiles especially for the cases of breaking waves when the global steepness is bigger than 0.35. The total energy at each position along the wave tank has larger values for steeper wave, beside the incipient wave case with $\epsilon = 0.35$ when $\epsilon < 0.6$. As for the extreme steep waves when the global wave steepness $\epsilon >= 0.6$, the energy increasing trend disturbs this phenomenon and shows more chaotic evolutions for the dissipation process in Fig. 23(b). This suggests that the wave energy and dissipation processes are more unsteady and have strong nonlinear profiles for extreme steep waves with the large global wave steepness.

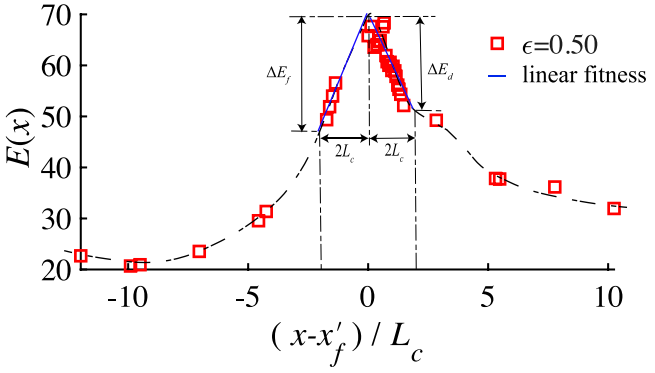

Fig. 24. Polynomial fitness of the energy spatial evolution.

The sketch definition of parameters for calculating the energy changing rate is depicted in Fig. 24. The energy spatial distribution of case WG5 $\epsilon = 0.5$ is taken as an example for the energy parameter definition. The variations of the energy within one local wavelength $L_b = 2L_c$ for the focusing and dissipation processes are defined as ΔE_f and ΔE_d separately. The variation of energy changing rate R within one local wavelength versus global wave steepness is shown in Fig. 25. The energy focusing rate is F_{rate} assigned as red circles and the dissipation rate is D_{rate} marked as blue squares in Fig. 25. The focusing energy rate F_{rate} and energy dissipation rate D_{rate} both satisfy the linear function as the increase of global wave steepness. The phenomenon of the increasing trend of energy dissipation rate versus increased global steepness is similar to the conclusion in Melville (1994). The focused waves with steeper wave slopes not only collect more energy but also have a larger energy-changing rate R. The slopes of these two linear functions of the energy changing rate R are different, which also proved the asymmetric profile of the breaking process. The linear fitness distribution suggests that the energy focusing and dissipation rate can both be good breaking indicators. if using the focusing energy rate as the dynamic breaking criterion, the threshold for the spilling breaking is around 9 J/s. However, if it changed as dissipation energy rate this value turns to 10.7 J/s. The ratio of slopes of linear fitness function of two energy changing processes is around 0.79, which is also plotted by fitting the ratio of F_{rate}/D_{rate} corresponding to each global steepness. The constant value of F_{rate}/D_{rate} indicates that the focusing energy and the energy focusing rate determine the energy dissipation rate to a certain extent.

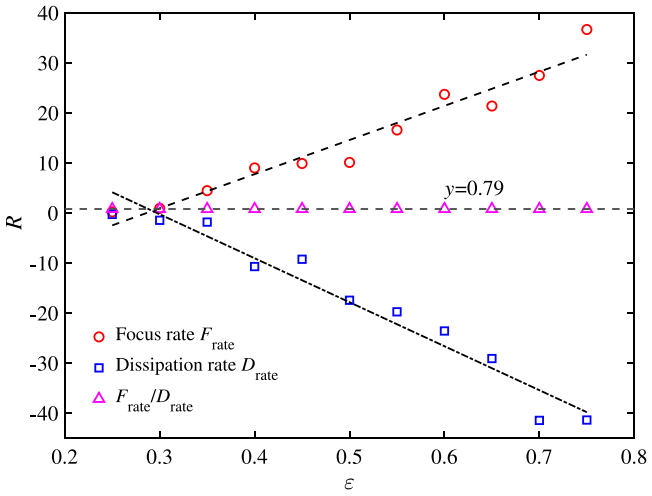

Fig. 25. Energy variation rate R versus global wave steepness.

4. Conclusions

The simulations of focused breaking waves with different breaking intensity have been performed in a two-phase numerical wave tank by solving the Navier–Stokes equations together with the level set method and the Large-eddy simulation turbulent model. The constant wave steepness method was employed to generate the focused breaking waves to study the variation of the wave geometry parameters, velocity and vorticity field, and the energy dissipation with different wave global steepness. Different wave breaking criteria were examined since the different breaking profiles and types were carried out with a large range of global wave steepness ε. The comparison of the wave elevation between the simulation and experimental results indicates that the numerical model can provide accurate and reliable simulation results. The detailed breaking profiles provided by the present numerical model is consistent with previous studies and give more insight views and understanding of the breaking process such as maximum velocity distribution, the generation and existence of the clockwise vortex and counterclockwise vortex, the air–water chaotic mixing phenomenon, and variation of turbulent intensity.

The focused position and time show a piecewise function as the increase of global steepness. The wave surface elevation envelope gives a reasonable explanation of the regular motion of the real focused position x'_f and focused time t'_f. As the increase of the global steepness, not only the amplitude of the focused position increased but also the neighbor wave envelope. The segmented variation of the focused position is due to the energy distribution method around the focused position. When the energy reached a balance between the focused wave envelope and the neighbors, the focused position will move upstreams abruptly. As another strong nonlinear element of the wave breaking, the air cavity under the impingement crest has been approximated by a $\sqrt{3}$-aspect ratio ellipse and the area of the air cavity shows a linear function of the global wave steepness. It also indicates that the breaking wave with large global steepness can carry and plunge more air into water and cause more chaotic air–water mixing.

The horizontal velocity has the maximum values during the breaking process at the impingement moment for each plunging breaking case. The vorticity field experienced a profile changing from simple to complex and chaotic during the breaking process. A counterclockwise vortex is generated between two positive vortexes rolling. The wave-breaking process may have a continued plunging process inducing more air–water mixing and energy dissipation. The generation of the vortexes and air–water mixing is the source of the turbulence kinetic energy dissipation. As the breaking crest propagates, the turbulence intensity increases at first and then decreases and gets a maximum value at the first splash-up scenario moment.

Three types of geometry parameters including Stokes breaking limitation, global wave steepness, and local wave parameters were calculated for geometry breaking criterion analysis. The breaking coefficient σ, which may depend on the breaker type, shows a linear functional relationship with the global wave steepness ε. $\sigma = 0.015$ could be a classification threshold of spilling and plunging breakers in this study. The global wave steepness as a typical geometry wave shape parameter has proved to be a stable and credible criterion to predict wave breaking. The threshold values of global wave steepness corresponding to different breaking profiles such as incipient, spilling and plunging breaker are in good agreement with the experimental results of Lamarre (1993). As for the local steepness parameters, the linear fitness trend of crest front steepness shows a relatively good prediction of wave breaking. The distributions of the other three local geometry parameters are relatively dispersed and irregular, and inappropriate as breaking criteria. The local steepness ε_b estimated by the local wave geometry profile shows a linear functional relationship with the global wave steepness: $\varepsilon_b = 1.12\varepsilon$. From the above summaries, the global steepness, as a pre-established and controllable geometry parameter, is a credible and practical criterion for wave-breaking prediction.

The kinematic breaking ratio $|\vec{U}|/C_p$ gives a good prediction of wave breaking and satisfies the kinematic breaking criterion $|\vec{U}|/C_p = 1$ in the present study. The breaking ratio has a time interval satisfying the breaking criterion $|\vec{U}|/C_p = 1$. The time interval when $|\vec{U}|/C_p > 1$ is different between the spilling and plunging breakers. The length of this time interval is related to the breaking type and intensity, so it may be an indicator to predict the breaking type. The breaking ratio at the incipient breaking scenario shows a cubic polynomial curve-fitting versus global wave steepness and the breaking ratio exists $|\vec{U}|/C_p < 1$ at the incipient section for some breaking cases until $\varepsilon >= 0.5$. So it proved that only using the values of breaking ratio at the incipient section as a judgment to predict wave breaking is not an accurate and sufficient method and criterion.

The variation of the total energy along the x-direction shows an apparent increasing trend as the increase of global wave steepness. The energy changing rate R defined by one local wavelength has been proposed and used as the dynamic breaking criterion. The energy changing rate R shows a linear function with the global wave steepness both for the focused and dissipation process. Compared with the previous dynamic breaking criterion which depends too much on wave probe location for energy estimation, the energy changing rate could be a good breaking indicator. The threshold of the energy focusing rate F_{rate} and dissipation rate D_{rate} for the spilling breaking are 9 J/s and 10.7 J/s separately.

Declaration of competing interest

The authors declare that they have no known competing financial interests or personal relationships that could have appeared to influence the work reported in this paper.

Acknowledgments

The authors are grateful for the grants provided by Lingshui Semi-submersible Production Platform Research Project no. LSZX-2020-HN-05-04. This research was supported with computational resources at NTNU provided by NOTUR (Norwegian Metacenter for Computational Sciences, http://www.notur.no) under project no. NN2620K. This study has also been partially carried out within the project of the Fundamental Research Funds for the Central Universities, China (HIT.OCEF. 2021037) and Taishan Scholars Project of Shandong Province (tsqn201909172).

Appendix A. Two phase model and numerical method

A.1. Two phase flow model

The governing equations mentioned above are solved for both the air and the water phases. The evolution of level set function in a fixed cell $\phi(\vec{x},t)$ are used to capture the interface and distinguish the air and water phases. The level set function as the signed distance function can be expressed as follows:

$$\frac{\partial \phi}{\partial t} + u_j \frac{\partial \phi}{\partial x_j} = 0, \tag{18}$$

and has the following properties:

$$\phi(\vec{x},t)\begin{cases} > 0 \; if \; \vec{x} \in Water \\ = 0 \; if \; \vec{x} \in \Gamma \\ < 0 \; if \; \vec{x} \in Air \end{cases} \tag{19}$$

The free surface Γ evolves as the time step forward by coupling with the velocity field generated by the momentum equation. When the surface Γ moved by the correct velocity field in Eq. (18), ϕ may lose its properties as a distance signed function at a new time step. Thus, to maintain its properties and ensure the mass conservation, the reinitialization of the level set function is required after each time step.

$$\frac{\partial \phi}{\partial t} + S(\phi)(\nabla |\phi| - 1) = 0, \tag{20}$$

here, $S(\phi)$ is the smoothed sign function (Peng et al., 1999)defined as $S(\phi) = \frac{\phi}{\sqrt{\phi^2 + (|\nabla \phi| \epsilon)^2}}$.

To overcome the instabilities and discontinuous materials problems, a Heaviside function is adopted to give a smoothed density and viscosity changing across the interface.

$$H(\phi_i) = \begin{cases} 0 & if \; \phi_i < -\epsilon \\ \frac{1}{2}\left(1 + \frac{\phi}{\epsilon} + \frac{1}{\pi}\sin\left(\frac{\pi \phi_i}{\epsilon}\right)\right) & if \; |\phi_i| \le \epsilon \\ 1 & if \; \phi_i > \epsilon. \end{cases} \tag{21}$$

The smoothed finite thickness is chosen as $\epsilon = 2.1\Delta x$ on both sides of the interface. The momentum equation is closed with the fluid density and viscosity constitution equations in the domain:

$$\rho_i = \rho_w H(\phi_i) + \rho_a (1 - H(\phi_i)), \tag{22}$$

$$\nu_i = \nu_w H(\phi_i) + \nu_a (1 - H(\phi_i)), \tag{23}$$

with w indicating water and a representing air properties. H is the smoothed Heaviside function in Eq. (21). The density is generally determined at the cell faces to get a more stable and accurate solution (Bihs et al., 2016).

A.2. Numerical method

The governing equations depicted above Eqs. (1) and (3) are solved with the application of the level set method and LES turbulence model on a finite-difference framework. A staggered rectilinear Cartesian grid is used in the two-phase flow model for the high-order spatial discretization schemes. A fifth-order accurate Weighted Essentially Non-oscillatory (WENO) scheme (Jiang and Shu, 1996) is adopted for the spatial discretization of convection terms in the non-uniform grid. The second-order accurate central differences are applied for discretion the diffusion terms. The time derivatives in Eqs. (3) and (18) are discretized by an accurate third-order Total Variation Diminishing (TVD) Runge–Kutta explicit time scheme developed by Harten (Shu and Osher, 1988).

In this study, an adaptive time step is selected based on the CFL number. When the CFL number is below 1, this time scheme shows good numerical stability and provides a high order of temporal accuracy. The time stepping method balances the stability of simulation and the requirement of the computational cost. According to velocity, diffusion, and the source term S, the time step size Δt_{CFL} can be defined as follows:

$$\Delta t_{CFL} \le 2\left(\left(\frac{|U|_{max}}{dx} + \nu_{eff} * \Delta\delta\right) + \sqrt{\left(\frac{|U|_{max}}{dx} + \nu_{eff} * \Delta\delta\right)^2 + \frac{4|S_{max}|}{dx}}\right)^{-1}, \tag{24}$$

where S is the source term, $|U|_{max} = \sqrt{u_{max}^2 + v_{max}^2 + w_{max}^2}$, $\nu_{eff} * \Delta\delta$ represents the contribution from the diffusion term, and $\Delta\delta = \min(dx, dy, dz)$. To calculate the details of the breaking process, the time step in this paper is automatically adjusted with the value of $0.1 * \Delta t_{CFL}$ during the simulation.

The pressure gradient is modeled by projection method (Chorin, 1968) for incompressible flow on the staggered grid. The momentum equation is solved explicitly without the pressure gradient term and the updated velocity after each time step is the predicted velocity u_i^*. The predicted velocity u_i^* will be inserted into the Poisson equation to calculate and update the pressure for the new time step.

$$-\frac{\partial}{\partial x_i}\left(\frac{1}{\rho(\phi^n)}\frac{\partial p}{\partial x_i}\right) = -\frac{1}{\Delta t}\frac{\partial u_i^*}{\partial x_i}, \tag{25}$$

The Poisson equation for the pressure is solved using the Bi-Conjugate gradients Stabilized (BiCGStab) struct solver with parallel fully multi-grid (PFMG) preconditioner available from the HYPRE solver library. Then the predicted velocity field will be corrected by the pressure and getting the divergence free velocity at the new time step:

$$u_i^{n+1} = u_i^* - \frac{\Delta t}{\rho(\phi^n)}\frac{\partial p}{\partial x_i}, \tag{26}$$

Appendix B. Grid convergency

The grid convergence study is performed by simulating the experimental focused nonbreaking case DF1 and breaking wave case DF2 with the grid size of $dx = 0.005$ m, 0.003 m, the stretching grid from 0.003 m to 0.001 m and 0.001 m. Fig. 26 presents the comparison of the wave surface elevation at the focused position with different grid sizes. The real focused point for case DF1 and DF2 are 7.1 m and 6.2 m respectively. The results in Fig. 26(a) show that the numerical values for the wave elevation at stretching grid and $dx = 0.001$ m are similar to each other compared to the results at grid size $dx = 0.005$ m and $dx = 0.003$ m. Fig. 26(b) shows the wave elevation at the focused point for case DF2 converge for the stretching grid. The focused wave crest height is used to calculate the grid convergence ratio (Stern et al., 2001). The grid convergence ratio defined as $R = \frac{D_{mf}}{D_{cm}}$, where D_{mf} is the difference of the crest values between the medium and fine grids, and D_{cm} respect the varies between the coarse and medium grids. The grid size 0.003 m, stretching grid from 0.003 m to 0.001 m, and 0.001 m are selected as coarse, medium and fine grids respectively. A convergence ratio of $R = 0.2$ is obtained for case DF1 and $R = 0.12$ for case DF2. Both these two values are within the range of the monotonic convergency for R and indicate that the selected grid size satisfies the convergency study.

The overturning processes for the steep breaking waves with global wave steepness as 0.7 simulated with stretching grid with a total of grid number 2.8 million grids and the fine grid $dx = 0.001$ m with a total of 15 million are presented in Figs. 27(a) and 27(b), respectively. The high-resolution simulation not only provides details on the front overturning crest kinematic feature but also captures the flow profile of the back of the splash-up. The stretching grid captures similar details like the high-resolution simulation around the front of the splash-up overturning. For the breaking wave, the front of the splash-up has more significance in wave–structure interaction. So there is no significant improvement in the results for the wave breaking details when the grid

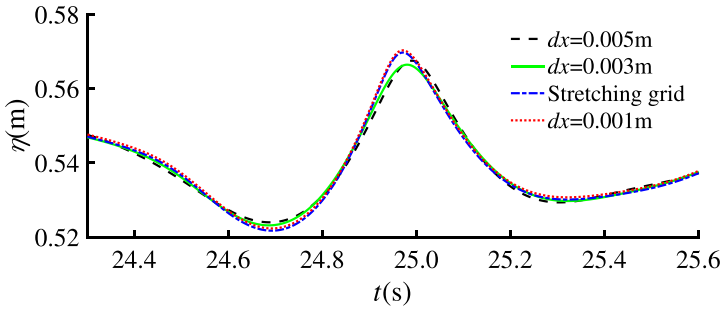

(a) Grid convergence study of the focusing wave with global wave steepness ε as 0.25

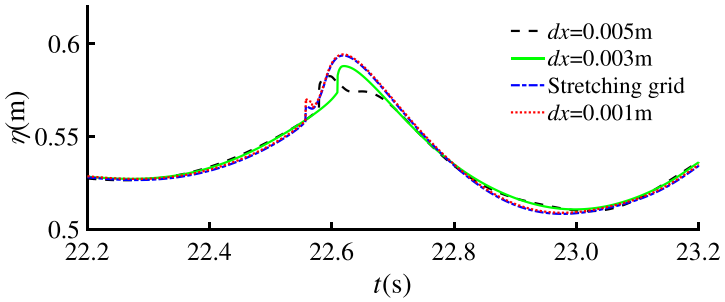

(b) Grid convergence study of the focused breaking wave with global wave steepness ε 0.57

Fig. 26. Grid convergence at the focused position.

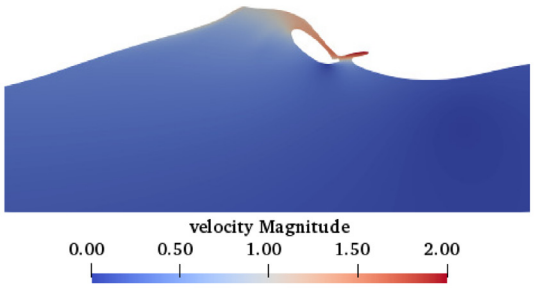

(a) Overturning process of focused breaking wave with stretching grid 0.003m to 0.001m and a total of 2.8 million grids

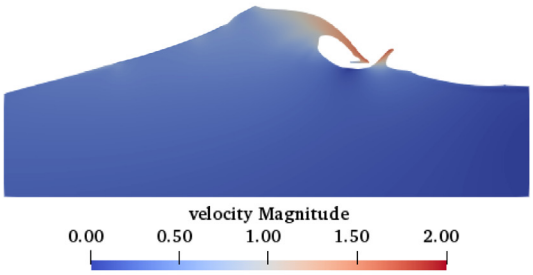

(b) Overturning process of focused breaking wave with $dx = 0.001m$ and a total of 15 million grids

Fig. 27. Overturning process of focused breaking wave for case WG9 with $\varepsilon = 0.70$ under different grid size.

size is refined from stretching grid to dx = 0.001 m. From the grid convergence study, the stretching grid is accurate for both no breaking and breaking cases, so the stretching grid is selected for simulation cases in this study.

References

Alagan Chella, M., Bihs, H., Myrhaug, D., 2015. Characteristics and profile asymmetry properties of waves breaking over an impermeable submerged reef. Coast. Eng. (ISSN: 0378-3839) 100, 26–36. http://dx.doi.org/10.1016/j.coastaleng.2015.03.008.

Alberello, A., Chabchoub, A., Monty, J.P., Nelli, F., Lee, J.H., Elsnab, J., Toffoli, A., 2018. An experimental comparison of velocities underneath focussed breaking waves. Ocean Eng. (ISSN: 0029-8018) 155, 201–210. http://dx.doi.org/10.1016/j.oceaneng.2018.02.049.

Alberello, A., Iafrati, A., 2019. The velocity field underneath a breaking rogue wave: Laboratory experiments versus numerical simulations. Fluids 4, 68.

Baldock, T.E., Swan, C., Taylor, P.H., 1996. A laboratory study of nonlinear surface waves on water. Philos. Trans. R. Soc. Lond. Ser. A Math. Phys. Eng. Sci. (ISSN: 1364503X) 354 (1707), 649–676.

Banner, M.L., Peregrine, D.H., 1993. Wave breaking in deep water. Annu. Rev. Fluid Mech. 25 (1), 373–397. http://dx.doi.org/10.1146/annurev.fl.25.010193.002105.

Bihs, H., Kamath, A., Alagan Chella, M., Aggarwal, A., Arntsen, Ø.A., 2016. A new level set numerical wave tank with improved density interpolation for complex wave hydrodynamics. Comput. & Fluids (ISSN: 0045-7930) 140, 191–208. http://dx.doi.org/10.1016/j.compfluid.2016.09.012.

Bonmarin, P., 1989. Geometric properties of deep-water breaking waves. J. Fluid Mech. 209, 405–433. http://dx.doi.org/10.1017/S0022112089003162.

Chorin, A.J., 1968. Numerical solution of the Navier-Stokes equations. Math. Comp. 22 (104), 745–762.

Drazen, D.A., Melville, W.K., Lenain, L., 2008. Inertial scaling of dissipation in unsteady breaking waves. J. Fluid Mech. 611, 307–332. http://dx.doi.org/10.1017/S0022112008002826.

Duncan, J.H., 2001. Spilling breakers. Annu. Rev. Fluid Mech. 33 (1), 519–547. http://dx.doi.org/10.1146/annurev.fluid.33.1.519.

Duncan, J.H., Longuet-Higgins, M.S., 1981. An experimental investigation of breaking waves produced by a towed hydrofoil. Proc. R. Soc. Lond. Ser. A Math. Phys. Eng. Sci. 377 (1770), 331–348. http://dx.doi.org/10.1098/rspa.1981.0127.

Duncan, J.H., Qiao, H., Philomin, V., Wenz, A., 1999. Gentle spilling breakers: Crest profile evolution. J. Fluid Mech. 379, 191–222. http://dx.doi.org/10.1017/S0022112098003152.

Gao, W., Cheng, W., Samtaney, R., 2020. Large-eddy simulations of turbulent flow in a channel with streamwise periodic constrictions. J. Fluid Mech. 900, A43. http://dx.doi.org/10.1017/jfm.2020.512.

Grue, J., Clamond, D., Huseby, M., Jensen, A., 2003. Kinematics of extreme waves in deep water. Appl. Ocean Res. 25, 355–366. http://dx.doi.org/10.1016/j.apor.2004.03.001.

Hodges, L.H., James, Caskey, 1962. General circulation experiments with the primitive equations I. The basic experiment.

Jacobsen, N.G., Fuhrman, D.R., Fredsøe, J., 2012. A wave generation toolbox for the open-source CFD library: OpenFoam®. Internat. J. Numer. Methods Fluids 70 (9), 1073–1088. http://dx.doi.org/10.1002/fld.2726.

Jiang, G.-S., Shu, C.-W., 1996. Efficient implementation of weighted ENO schemes. J. Comput. Phys. (ISSN: 0021-9991) 126 (1), 202–228. http://dx.doi.org/10.1006/jcph.1996.0130.

Kway, J.H.L., Loh, Y.-S., Chan, E.-S., 1998. Laboratory study of deep-water breaking waves. Ocean Eng. (ISSN: 0029-8018) 25 (8), 657–676. http://dx.doi.org/10.1016/S0029-8018(97)00039-5.

Lamarre, E., 1993. An Experimental Study of Air Entrainment By Breaking Waves (Ph.D. thesis). Massachusetts Institute of Technology.

Lamarre, É., Melville, W.K., 1991. Air entrainment and dissipation in breaking waves. Nature 351, 469–472.

Lim, H.-J., Chang, K.-A., Huang, Z.-C., Na, B., 2015. Experimental study on plunging breaking waves in deep water. J. Geophys. Res. Oceans 120 (3), 2007–2049. http://dx.doi.org/10.1002/2014JC010269.

Longuet-Higgins, M.S., 1969. On wave breaking and the equilibrium spectrum of wind-generated waves. Proc. R. Soc. A (ISSN: 00804630) 310 (1501), 151–159.

Lubin, P., Glockner, S., 2015. Numerical simulations of three-dimensional plunging breaking waves: Generation and evolution of aerated vortex filaments. J. Fluid Mech. 767, 364–393. http://dx.doi.org/10.1017/jfm.2015.62.

Mayer, S., Garapon, A., Sørensen, L.S., 1998. A fractional step method for unsteady free-surface flow with applications to non-linear wave dynamics. Internat. J. Numer. Methods Fluids 28 (2), 293–315. http://dx.doi.org/10.1002/(SICI)1097-0363(19980815)28:2<293::AID-FLD719>3.0.CO;2-1, cited By 150.

Melville, W.K., 1994. Energy dissipation by breaking waves. J. Phys. Oceanogr. 24 (10), 2041–2049. http://dx.doi.org/10.1175/1520-0485(1994)024<2041:EDBBW>2.0.CO;2.

Melville, W.K., 1996. The role of surface-wave breaking in air-sea interaction. Annu. Rev. Fluid Mech. 28 (1), 279–321. http://dx.doi.org/10.1146/annurev.fl.28.010196.001431.

Na, B., Chang, K.-A., Lim, H.-J., 2020. Flow kinematics and air entrainment under laboratory spilling breaking waves. J. Fluid Mech. 882, A15. http://dx.doi.org/10.1017/jfm.2019.817.

Nadaoka, K., Hino, M., Koyano, Y., 1989. Structure of the turbulent flow field under breaking waves in the surf zone. J. Fluid Mech. 204, 359–387. http://dx.doi.org/10.1017/S0022112089001783.

New, A.L., 1983. A class of elliptical free-surface flows. J. Fluid Mech. 130, 219–239. http://dx.doi.org/10.1017/S0022112083001068.

Peng, D., Merriman, B., Osher, S., Zhao, H., Kang, M., 1999. A PDE-based fast local level set method. J. Comput. Phys. 155.

Perlin, M., Choi, W., Tian, Z., 2013. Breaking waves in deep and intermediate waters. Annu. Rev. Fluid Mech. 45 (1), 115–145. http://dx.doi.org/10.1146/annurev-fluid-011212-140721.

Perlin, M., He, J., Bernal, L.P., 1996. An experimental study of deep water plunging breakers. Phys. Fluids 8 (9), 2365–2374. http://dx.doi.org/10.1063/1.869021.

Ramberg, S.E., Griffin, O.M., 1987. Laboratory study of steep and breaking deep water waves. J. Waterw. Port Coast. Ocean Eng. 113 (5), 493–506. http://dx.doi.org/10.1061/(ASCE)0733-950X(1987)113:5(493).

Rapp, R.J., Melville, W.K., Longuet-Higgins, M.S., 1990. Laboratory measurements of deep-water breaking waves. Phil. Trans. R. Soc. A 331 (1622), 735–800. http://dx.doi.org/10.1098/rsta.1990.0098.

Shu, C.-W., Osher, S., 1988. Efficient implementation of essentially non-oscillatory shock-capturing schemes. J. Comput. Phys. (ISSN: 0021-9991) 77 (2), 439–471. http://dx.doi.org/10.1016/0021-9991(88)90177-5.

Song, J.-B., Banner, M.L., 2002. On determining the onset and strength of breaking for deep water waves. part I: Unforced irrotational wave groups. J. Phys. Oceanogr. 32 (9), 2541–2558. http://dx.doi.org/10.1175/1520-0485(2002)032<2541:ODTOAS>2.0.CO;2.

Stansell, P., MacFarlane, C., 2002. Experimental investigation of wave breaking criteria based on wave phase speeds. J. Phys. Oceanogr. 32 (5), 1269–1283.

Stern, F., Wilson, R., Coleman, H., Paterson, E., 2001. Comprehensive approach to verification and validation of CFD simulations—Part 1: Methodology and procedures. J. Fluids Eng. 123, 792. http://dx.doi.org/10.1115/1.1412235.

Tian, Z., Choi, W., 2013. Evolution of deep-water waves under wind forcing and wave breaking effects: Numerical simulations and experimental assessment. Eur. J. Mech. B/Fluids (ISSN: 0997-7546) 41, 11–22. http://dx.doi.org/10.1016/j.euromechflu.2013.04.001.

Tian, Z., Perlin, M., Choi, W., 2010. Energy dissipation in two-dimensional unsteady plunging breakers and an eddy viscosity model. J. Fluid Mech. 655, 217–257. http://dx.doi.org/10.1017/S0022112010000832.

Tian, Z., Perlin, M., Choi, W., 2012. An eddy viscosity model for two-dimensional breaking waves and its validation with laboratory experiments. Phys. Fluids 24 (3), 036601. http://dx.doi.org/10.1063/1.3687508.

Wu, C.H., Nepf, H.M., 2002. Breaking criteria and energy losses for three-dimensional wave breaking. J. Geophys. Res. Oceans 107 (C10), 41–1–41–18. http://dx.doi.org/10.1029/2001JC001077.